

DYNAMICAL EQUILIBRIUM PRESSURE IN
CLUSTER AND FIELD GALAXIES

THE ROLE OF DYNAMICAL EQUILIBRIUM PRESSURE IN THE
DIFFERENT MOLECULAR GAS RATIOS AND STAR
FORMATION PROPERTIES OF CLUSTER GALAXIES AND
FIELD GALAXIES

By TAAVISHI JINDEL, BSc.

A Thesis Submitted to the School of Graduate Studies in Partial
Fulfillment of the Requirements for
the Degree Master of Science

McMaster University © Copyright by Taavishi Jindel, September

2024

McMaster University

MASTER OF SCIENCE (2024)

Hamilton, Ontario, Canada (Physics and Astronomy)

TITLE: The role of dynamical equilibrium pressure in the different molecular gas ratios and star formation properties of cluster galaxies and field galaxies

AUTHOR: Taavishi Jindel
BSc. Honors (Physical Sciences: Physics),
Yale-NUS College, Singapore

SUPERVISOR: Dr. Christine Wilson

NUMBER OF PAGES: xii, 70

Abstract

The environment of a galaxy influences its gas and star formation properties via evolutionary mechanisms, such as ram pressure stripping and tidal stripping. In particular, the molecular to atomic gas ratio and dynamical equilibrium pressure are key parameters for understanding star formation in galaxies. I use 1.2 kpc data for galaxies in the Virgo Cluster from the VERTICO survey and for field galaxies from the HERACLES survey to study the spatially resolved relationship between molecular to atomic gas ratios and star formation properties (eg. star formation rate, molecular gas depletion time) in galaxies as a function of dynamical equilibrium pressure. I find that cluster galaxies have higher molecular to atomic gas ratios at a given dynamical equilibrium pressure than field galaxies do. Within both samples there is strong galaxy to galaxy variation in the relationship driven by the gas content of each galaxy. In order to investigate the role of cluster environmental mechanisms on the properties of cluster galaxies I use atomic gas deficiency as a proxy for these environmental mechanisms. I find that atomic gas deficiency plays a significant role in the gas properties, star formation properties and dynamical equilibrium pressure of cluster galaxies.

Acknowledgements

I would like to thank my supervisor Dr. Christine Wilson for the opportunity to pursue my dream of working in Astronomy. Thank you for your continuous support and guidance throughout the years. I look forward to continuing to do research with you for the years to come. I would also like to thank my committee members Dr. Laura Parker and Dr. Ralph Pudritz for their valuable feedback throughout the process. Thank you to Dr. Toby Brown, Dr. Sara Ellison, and Dr. Jiayi Sun for their insightful discussions and technical support.

Thank you to my friends at McMaster, Nicole, Megan, Jennifer, Claude, Veronika, Jeremy and Kate, for making the department a welcoming and fun environment for me. I am grateful to be surrounded by such passionate and gifted astronomers. I would also like to thank Blake for always patiently answering my questions and providing me with thoughtful advice.

I am also immensely grateful for my friends in Canada, Kate, Bridget, Selina, Adela, Debbie, Judith, and Amanda, who went out of their way to make this new country feel like home for me. Thank you for supporting me through everything, and being my family away from home. I would also like to thank Dr. Defne, Dr. Pinar, Dr. Metrie and Dr. Sharon for believing in me. I hope to one day have your levels of wisdom, compassion, and scientific expertise. Thank you to Tabitha, Jasmine, and

Vashita without whom I would not still be here. Thank you for constantly making me feel loved even from across the globe. Most of all I would like to thank my mom, dad, and sister. Thank you for being my rock when things are rough, loving me unconditionally, and always believing in me. Everything I do is because of the three of you. To all my friends and family, thank you for being there for me and always making me feel valued through sickness and through health.

Table of Contents

Abstract	iii
Acknowledgements	iv
Abbreviations	xi
1 Introduction	1
1.1 The Cold Interstellar Gas of Galaxies	2
1.1.1 Molecular Gas	2
1.1.2 Atomic Gas	5
1.2 Star Formation in Galaxies	6
1.3 Galaxies and their Environments	9
1.3.1 Field Galaxies	10
1.3.2 Galaxies in Clusters	10
1.3.3 The Virgo Cluster	13
1.4 The role of pressure in the Interstellar Gas	15
1.4.1 Turbulent Pressure	15
1.4.2 Dynamical Equilibrium Pressure	16
1.5 This Thesis	18

1.5.1	Motivation for this Thesis	18
1.5.2	Outline for this Thesis	21
2	Observational Data and Methods	22
2.1	Field Galaxies Sample	22
2.2	Cluster Galaxies Sample	24
2.3	Dynamical Equilibrium Pressure Calculation	29
2.4	Dynamical Equilibrium Pressure vs. a Proxy for Pressure	33
2.5	Other Properties	34
3	Results	36
3.1	Molecular to Atomic Gas Ratio vs. Dynamical Equilibrium Pressure	36
3.2	Star Formation Rate vs. Dynamical Equilibrium Pressure	44
3.3	Molecular Gas Depletion Time vs. Dynamical Equilibrium Pressure .	47
3.4	Global Stellar Mass Comparison of Samples	51
4	Conclusions & Future Work	54
4.1	Results of this thesis	54
4.2	Future Work	56
A	R_{mol} vs. P_{DE} for Individual Galaxies	59

List of Figures

1.1	The resolved Kennicutt-Schmidt relation for galaxies in VERTICO	8
1.2	Composite image of the Virgo Cluster from VERTICO	14
1.3	Molecular gas ratio vs. dynamical equilibrium pressure for 14 galaxies from Blitz & Rosolowsky (2006)	19
2.1	The global molecular gas mass vs. the global stellar mass of galaxies in the cluster and field samples of this thesis	28
2.2	The global star formation rate vs. the global stellar mass of galaxies in the cluster and field samples of this thesis	29
2.3	A comparison of dynamical equilibrium pressure with the pressure proxy across atomic gas deficiencies	34
3.1	Molecular gas ratio vs. dynamical equilibrium pressure of cluster galaxies vs. field galaxies	37
3.2	Field galaxy case-study: NGC 3521	38
3.3	Cluster galaxy case-study: NGC 4569	38
3.4	Role of atomic gas deficiency in molecular gas ratio vs. dynamical equilibrium pressure of field galaxies vs. cluster galaxies	39
3.5	Star formation rate surface density vs. dynamical equilibrium pressure of cluster galaxies vs. field galaxies	44

3.6	Star formation rate surface density vs. dynamical equilibrium pressure of galaxies from Ellison et al. (2024)	45
3.7	Role of atomic gas deficiency in star formation rate surface density vs. dynamical equilibrium pressure of cluster galaxies vs. field galaxies	46
3.8	Molecular gas depletion time vs. dynamical equilibrium pressure of cluster galaxies vs. field galaxies	47
3.9	Depletion time vs. radius from EDGE-CALIFA survey (Utomo et al., 2017)	48
3.10	Role of atomic gas deficiency in molecular gas depletion time vs. dynamical equilibrium pressure of field galaxies vs. cluster galaxies	49
3.11	Sample stellar mass cut of $M_{\odot} = 10^{10}$	52
3.12	Results with stellar mass restricted samples	53
A.1	Molecular gas to atomic gas ratio vs. dynamical equilibrium pressure for every galaxy in the field sample at 1.2 kpc resolution	59
A.2	Molecular gas to atomic gas ratio vs. dynamical equilibrium pressure for every galaxy in the cluster sample at 1.2 kpc resolution	60

List of Tables

2.1	Field galaxy sample overview	23
2.2	Cluster galaxy sample overview	27

Abbreviations

ISM	Interstellar medium
R_{mol}	Molecular gas to atomic gas ratio
PHANGS	Physics at High Angular resolution in Nearby Galaxies
GMC	Giant molecular cloud
CO	Carbon monoxide molecule
CO(1-0)	The lowest energy level transition of the CO molecule
VLA	Very Large Array
ALMA	Atacama Large Millimeter Array
THINGS	The HI Nearby Galaxy Survey
def_{HI}	Atomic gas deficiency
rms	Root mean square
IRAM	Institut de Radioastronomie Millimétrique
WISE	Wide-field Infrared Survey Explorer 2 and 3

WISE1	WISE at 3.4 microns
WISE2	WISE at 4.6 microns
WISE3	WISE at 12 microns
WISE4	WISE at 22 microns
GALEX	Galaxy Evolution Explorer
NUV	Near-ultraviolet

Chapter 1

Introduction

Galaxies are gravitationally bound systems of dust, gas and stars surrounded by a dark matter halo. The interstellar gas of galaxies fuels the star formation in galaxies, which causes stellar feedback that consequently influences the gas properties. This gas-star formation cycle determines many of the properties of galaxies and their evolution.

There are, therefore, many gas-centric models in galaxy evolution that are based on the matter cycle (Dekel et al., 2009; Davé et al., 2011; Lilly et al., 2013). The fundamental components of these models are the gas inflow rate into a galaxy, the star formation rate, and the outflow of gas from the galaxy (Saintonge et al., 2018). These models demonstrate the crucial role that gas plays in the field of galaxy evolution (Leroy et al., 2008; Lilly et al., 2013; Kennicutt & Evans, 2012).

1.1 The Cold Interstellar Gas of Galaxies

The interstellar medium (ISM) of a galaxy is the gas and dust component of the galaxy that exists in between the stars. It has a wide range of temperatures and densities. The ISM contains three components in pressure equilibrium: the cold neutral medium, the warm neutral medium and the hot ionized medium (McKee & Ostriker, 1977; Cox, 2005; Saintonge & Catinella, 2022). It also contains a molecular phase that is out of pressure equilibrium. The cold neutral and molecular ISM is the area of interest for this thesis. This is because, these phases together are the most massive component of the ISM, and because star formation occurs in this cold, dense phase of the interstellar medium. The cold ISM typically consists of 10% to 20% of the baryonic mass of a star forming galaxy, and less than 3% of the baryonic mass for early type galaxies (Davis et al., 2013; Saintonge & Catinella, 2022). Less than 1% of the cold ISM is made up of dust (Saintonge & Catinella, 2022). The breakdown of the cold interstellar gas into the atomic and molecular gas components varies from galaxy to galaxy as well as spatially within galaxies. A valuable parameter to study the phase breakdown of the cold interstellar gas is the ratio of the molecular gas mass surface density to the atomic gas mass surface density ($R_{mol} = \Sigma_{mol}/\Sigma_{HI}$).

1.1.1 Molecular Gas

The molecular phase of the cold interstellar medium is dominated by molecular Hydrogen (H_2). The molecular gas component of the galaxy is typically more concentrated than the atomic gas component (Davis et al., 2013). H_2 is difficult to observe, despite being the most commonly found molecule in the interstellar medium. This is because

it is symmetric and has a dipole moment of 0. This observational challenge is exacerbated at the lower temperatures at which molecular clouds occur. Carbon monoxide (CO) is the second most abundant molecule in molecular clouds, and therefore CO emission lines are the most commonly used tracer of molecular hydrogen (Bolatto et al., 2013).

CO(1-0) is the lowest energy transition of the CO molecule. It corresponds to the rotational transition of $J = 1 \rightarrow 0$, has a wavelength of 2.6 mm, occurs at $h\nu/k_B = 5.5\text{K}$, and has an approximate critical density of 3000 cm^{-3} (Saintonge & Catinella, 2022). h is the Planck constant, k_B is the Boltzmann constant, and ν is the frequency of the transition. The excitation for the rotational levels of CO molecules occurs from collisions with H_2 . The critical density of CO is the density at which the collisions of CO with H_2 are sufficiently frequent relative to the spontaneous decay rate, such that the excitation temperature of the rotational level approaches the kinetic temperature of the gas (Scoville, 2013, e.g.). Molecular gas typically has a temperature range of 10 K to 50 K, and characteristic densities of $10^2 - 10^5\text{ cm}^{-3}$, making the CO(1-0) emission line an effective tracer of molecular gas (Draine, 2011). The Earth's atmosphere is also relatively transparent at the CO(1-0) emission line, which makes it observable through ground-based telescopes, such as the Atacama Large Millimeter/submillimeter Array (ALMA) (e.g. Saintonge & Catinella, 2022). Other, higher energy emission lines of CO are also commonly used tracers of H_2 . One such example is CO(2-1), which has an approximate frequency of 230 GHz (Condon & Ransom, 2016).

The molecular gas mass is obtained from CO line luminosity (Solomon et al., 1997) by applying a conversion factor (α_{CO}). Extensive observational work has been done to

determine the optimal value of α_{CO} (Israel, 1997; Accurso et al., 2017; Bolatto et al., 2013; Tacconi et al., 2020). Despite these efforts, the conversion factors of CO lines still have a high level of uncertainty (Bolatto et al., 2013). ALMA led to immense progress in the spatially resolved mapping of molecular gas for local galaxies. This is because ALMA can produce a CO(2-1) map of a galaxy in a few hours (Schinnerer & Leroy, 2024). For example, the PHANGS-ALMA Survey (Leroy et al., 2021) observed the CO(2-1) line for 90 galaxies at a spatial resolution range sensitive to molecular clouds (50-150 pc).

The structure of molecular gas is complex, and reflects a balance between stellar feedback in the form of turbulence and winds as well as the self-gravity of the gas (Schinnerer & Leroy, 2024). Approximately 50% of molecular gas in the ISM is considered to occur in distinct bodies called molecular clouds of mass 10^4 - $10^6 M_{\odot}$ (Sawada et al., 2012; Blitz, 1993) under typical conditions. Originally, molecular clouds were considered to have a mean column molecular gas density of 10^{22} cm^{-2} and a clear dependence of line width on the size-scale of the clouds (Larson, 1981; Scoville et al., 1987; Blitz, 1993). It was, therefore also assumed that the dynamical mass of the cloud could be reliably inferred from the CO line emission characteristics, such as intensity and line width (Bolatto et al., 2008; Fukui & Kawamura, 2010).

However, recent surveys have led to a far more complex picture of molecular gas structures. The line width and surface density of molecular gas have been found to vary significantly across galaxies, and even within galaxies (Heyer et al., 2009; Heyer & Dame, 2015; Hughes et al., 2013a; Sun et al., 2018, 2020b). The properties of molecular clouds have been found to be a reflection of the properties of their host galaxy. The previously assumed clear relationship between the CO line width and

size of the molecular gas cloud, therefore, does not exist (Sun et al., 2018). Instead, the Heyer-Keto relation (Heyer et al., 2009; Keto & Myers, 1986) has become central to the study of the structure of molecular clouds. The Heyer-Keto relation is the relationship between the line width at a specific spatial scale, and the surface density of a gravitationally bound object (Heyer et al., 2009; Keto & Myers, 1986). It applies to molecular clouds because they are approximately gravitationally bound by self-gravity in a diverse range of environments (Heyer & Dame, 2015; Sun et al., 2020a; Saintonge & Catinella, 2022).

1.1.2 Atomic Gas

The atomic gas (HI) component of the interstellar medium is the most diffuse component of the neutral interstellar medium with a density of 0.6 cm^{-3} . It has temperatures of 100 K to 5000 K, and is typically more loosely bound and extended than the molecular gas component (Zabel et al., 2022). HI is the most abundant atom that exists. It has an emission line at 21.106 cm, at a frequency 1.420 GHz (Saintonge & Catinella, 2022). Most HI 21 cm observations of galaxies are global, which means they are spatially unresolved. Global measurements of the 21 cm HI line provide us with relatively accurate redshifts, doppler broadening estimates, and total HI masses (Saintonge & Catinella, 2022).

Spatially resolved HI measurements are difficult to obtain because of the relatively long wavelength of HI. The longer the wavelength of emission the larger the telescope needs to be to obtain spatially resolved measurements of the emission. The advent of radio interferometers such as the Very Large Array (VLA) led to spatially resolved HI maps for samples of star-forming galaxies at a maximum distance of 100 Mpc away.

One such survey is the HI Nearby Galaxy Survey (THINGS) that provided spatially resolved HI 21 cm observations for 34 galaxies at 3 to 15 Mpc (Walter et al., 2008).

Molecular gas forms from atomic gas. Atomic gas is, therefore the fuel for molecular gas reservoirs, and an indirect fuel for star formation (Kennicutt & Evans, 2012; Blitz & Rosolowsky, 2004, 2006; Krumholz et al., 2005; Zabel et al., 2022). While the conversion process from atomic gas to molecular gas is not well understood, there is strong evidence that pressure plays an important role (Blitz & Rosolowsky, 2004, 2006). This role of pressure is discussed further in Section 1.5.1. Atomic gas deficiency is a valuable parameter that is used in the study of the role of the environment on the atomic gas content of galaxies. For a discussion of atomic gas deficiency refer to Section 1.3.2.

1.2 Star Formation in Galaxies

When estimating star formation for highly resolved regions at cloud scales, single stellar populations of stars of the same age are considered (Schinnerer & Leroy, 2024). However, for measurements of star formation rate over regions greater than 1 kpc, which is the focus of this thesis, an average estimate of SFR over the region is usually calculated (Kennicutt & Evans, 2012; Sánchez, 2020). In order to obtain balanced estimates of SFR a combination of different types of emission is used. Each type of emission is sensitive to a different type of stellar population.

Ultraviolet emission is used to trace young stars. 90% of near-ultraviolet (NUV) emission is from stars younger than 200 Myrs (Kennicutt & Evans, 2012), and 90% of far-ultraviolet (FUV) emission is from stars younger than 100 Myrs (Kennicutt & Evans, 2012). The Galaxy Evolution Explorer (Martin & GALEX Team, 2005) has

significantly advanced the field by providing both NUV (230 nm) and FUV (155 nm) observations for approximately two-thirds of the sky. GALEX has thereby provided SFR estimates for over 100000 galaxies in a variety of galactic environments. The main disadvantage of ultraviolet emission as a tracer for star formation rates is that it is sensitive to dust attenuation. The recent availability of extensive infrared observations has made it easier to tackle this issue. Infrared/ UV emission ratios have been used to take into account the impact of dust attenuation (Kennicutt & Evans, 2012).

H α is another common SFR tracer. It is used to estimate the number of massive stars, as it traces the ionized gas that surrounds them. 90% of the stars that contribute to H α emission are younger than 10 Myrs. Lyman-alpha (Ly α) is used primarily to identify samples of star-forming galaxies at high redshifts. This is because Ly α emission has a higher intensity than H α emission. However, because Ly α is strongly quenched in typically interstellar medium conditions, H α is still the preferable tracer for closer galaxies (Kennicutt & Evans, 2012).

The star formation surface density (Σ_{SFR}), and molecular gas density Σ_{mol} are linked together through empirical scaling relationships such as the resolved Kennicutt-Schmidt relation (Schmidt, 1959; Kennicutt, 1998; Kennicutt & Evans, 2012). These relationships highlight the role of molecular gas as the fuel for star formation. The resolved Kennicutt-Schmidt relationship (Schmidt, 1959; Kennicutt, 1998; Kennicutt & Evans, 2012) links Σ_{mol} and (Σ_{SFR}) through the relationship (Bigiel et al., 2008; Leroy et al., 2013; Utomo et al., 2017):

$$\Sigma_{SFR} \propto \Sigma_{mol}^N \tag{1.2.1}$$

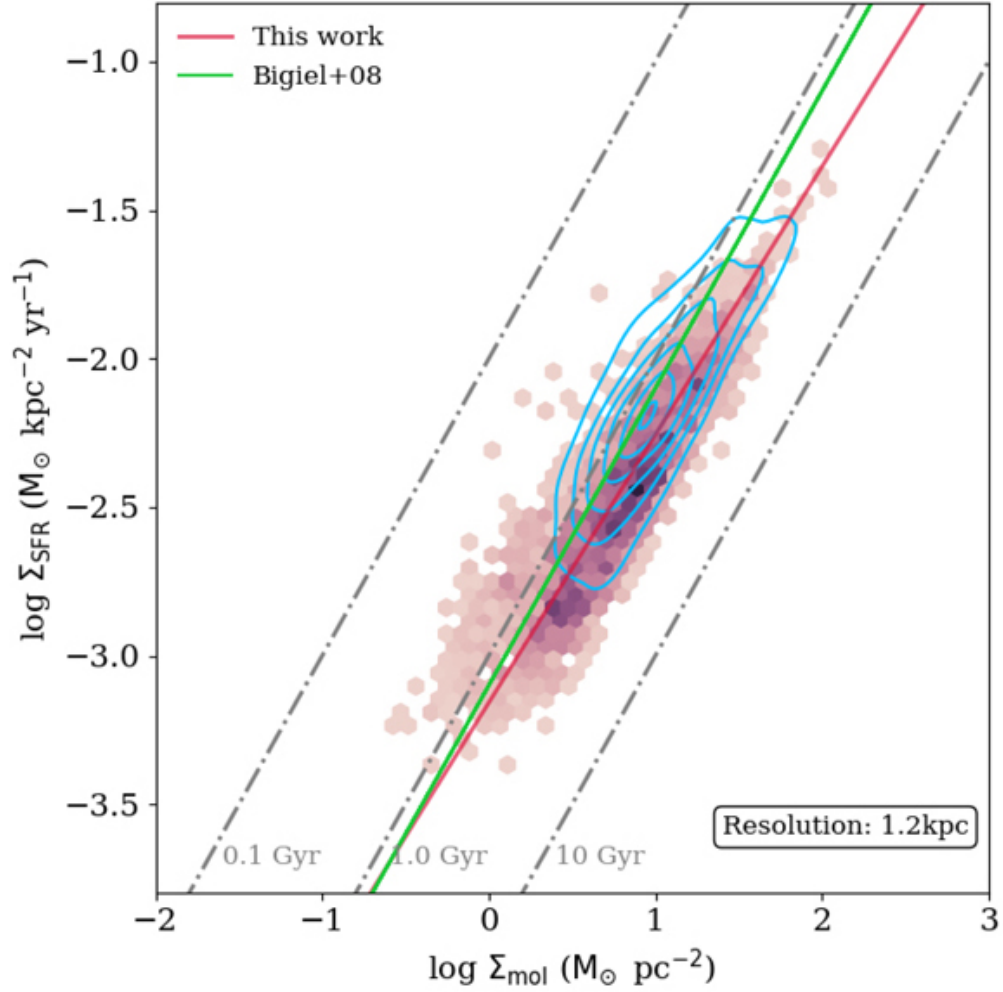


Figure 1.1: The resolved Kennicutt-Schmidt relation for galaxies in VERTICO at 1.2 kpc resolution. The data points represent the 1.2 kpc data for the VERTICO sample studied by Jiménez-Donaire et al. (2023). The best-fit line for these galaxies is represented by the red line. The green line is the best-fit line for the Kennicutt-Schmidt relation calculated by Bigiel et al. (2008). The blue contour lines represent the resolved data from galaxies from the HERA CO-Line Extra-galactic Survey. The black dashed lines represent constant molecular gas depletion times. Image credit: Jiménez-Donaire et al. (2023)

The resolved Kennicutt-Schmidt has been confirmed by many observational studies (Bigiel et al., 2008; Leroy et al., 2013; Lin et al., 2019). Figure 1.1 shows the resolved Kennicutt-Schmidt relation for 51 galaxies in the Virgo Environment Traced

in CO (VERTICO) survey at 1.2 kpc (Jiménez-Donaire et al., 2023). The best-fit line (red) of the Kennicutt-Schmidt relation found by Jiménez-Donaire et al. (2023) has a slope of 0.91 ± 0.08 . In addition, the resolved star-forming main sequence links together the stellar mass surface density, Σ_{M_*} and the star formation surface density Σ_{SFR} , through a linear or sub-linear relationship: (Sánchez et al., 2013; Cano-Díaz et al., 2016; Hsieh et al., 2017; Enia et al., 2020; Baker et al., 2022):

$$\Sigma_{SFR} \propto \Sigma_{M_*}^N \tag{1.2.2}$$

The efficiency at which gas is consumed to produce stars is an important parameter for understanding galaxy physics. Combining resolved gas measurements with resolved star formation estimates in the form of molecular gas depletion times ($\tau_{mol} = \Sigma_{mol}/\Sigma_{SFR}$) gives us useful physical timescales through which to understand the matter cycle that drives galaxy evolution.

1.3 Galaxies and their Environments

The environment that a galaxy occurs in has been found to impact the properties of the galaxy (Dressler, 1984). The role that the galaxy environment plays in galaxy evolution is, therefore, a valuable and active area of research (Zabel et al., 2022). Galaxy environments can be classified into two categories. The first is galaxy clusters, which are high-density environments discussed in Section 1.3.2. The second environment is the field. For this thesis we consider all galaxies that do not occur in clusters to be field galaxies, which are discussed in Section 1.3.1.

1.3.1 Field Galaxies

In this thesis we consider all galaxies that do not occur in clusters to be field galaxies. This includes galaxies that are relatively isolated from other galaxies, and have, therefore, not experienced recent interactions with other galaxies. This classification of field galaxies also includes galaxies that occur in groups. Groups of galaxies contain 3 to 50 galaxies, and galaxies usually have some evidence of recent interaction (Eke et al., 2005). Field galaxies allow us to study how galaxies evolve without the impact of high-density environments discussed in Section 1.3.2. The difference in properties between field galaxies and cluster galaxies is discussed in Section 1.3.2.

1.3.2 Galaxies in Clusters

Galaxy clusters comprise from 50 to 1000s of galaxies, extremely hot gas in between the galaxies, and a dark matter halo that surrounds the cluster (Oemler, 1974; Dressler, 1984; Zabel et al., 2022). The pervasive hot and diffuse gas in galaxy clusters is known as the intracluster medium. The intracluster medium has a characteristic temperature range of 10^7 - 10^8 K, a density of 10^{-4} cm^{-3} and emits in the X-ray region (Kaiser, 1986; White et al., 1997; Brown et al., 2021). The intracluster medium is dominated by ionized hydrogen and helium (Molendi et al., 2016). Galaxy clusters are frequently referred to as laboratories for the study of the role of environment in galaxy evolution (Brown et al., 2021).

Galaxies in clusters exhibit different properties from field galaxies, demonstrating that galaxies in clusters undergo a different evolution process than field galaxies. Dressler (1980) found that clusters have a significantly higher proportion of elliptical galaxies than field galaxies do. Furthermore, galaxies in clusters are typically

quenched, and therefore are more passive than the field galaxy population (Oemler, 1974; Dressler, 1984; Goto et al., 2003). This means that they have lower star formation rates and are redder than field galaxies. The properties of galaxies in a cluster also vary based on their location inside the cluster. The centers of galaxy clusters have higher numbers of large, red elliptical galaxies than the regions of the cluster radially further away from the center (Postman et al., 2005).

Galaxies in clusters experience a wide range of environmental mechanisms that cause them to be more passive than field galaxies (Balogh et al., 1998; Gómez et al., 2003; Boselli & Gavazzi, 2006; Brown et al., 2021). For example, galaxies in clusters experience ram pressure stripping. This is caused by the interaction of the intracluster medium and the interstellar medium of the galaxy. Frequently, the movement of the galaxy through the intracluster medium causes the cold gas of the galaxy to be stripped away (Gunn & Gott, 1972; Hester, 2006; Fujita & Sarazin, 2001). Ram pressure stripping may also cause elevated gas densities, which impacts both the star formation efficiency and the conversion of atomic gas in the ISM to molecular gas (Lee et al., 2017; Mok et al., 2017; Moretti et al., 2020).

The interaction of a galaxy with the hot diffuse intracluster medium of the cluster can cause the galaxy to be environmentally quenched in two different ways. The first quenching mechanism is if during the infall of a galaxy in a cluster the hot gas in the galaxy halo is removed (Larson et al., 1980; Balogh et al., 2000). The second mechanism that can occur is if the hot gas in the halo of a galaxy is unable to cool down due to its interaction with the hot cluster intracluster medium (Balogh et al., 2000). The consequence of both these quenching mechanisms is that the cold gas of the galaxy consumed in star formation does not get replenished. This causes the star formation

of the galaxy to be suppressed (Bekki et al., 2002). Quenching can also arise from the high velocity interactions of galaxies with each other. These interactions can cause the gas of the galaxy to tidally heat up, reducing cold gas reservoirs and quenching star formation (Moore et al., 1996, 1998, 1999; Fujita, 1998). Because environmental mechanisms impact the atomic gas and molecular gas of cluster galaxies in different ways we would expect the environmental mechanisms to influence the R_{mol} of cluster galaxies. Cluster galaxies would, therefore, have different R_{mol} values relative to field galaxies.

Atomic Gas Deficiency

Atomic gas is the most extended and loosely bound component of the interstellar medium. This makes it more susceptible to being removed from galaxies by environmental mechanisms (Haynes et al., 1984; Verheijen & Sancisi, 2001; Zabel et al., 2022). As a result, galaxies in clusters tend to have a reduced amount of atomic gas relative to field galaxies of a similar size and type (Chamaraux et al., 1970; Giovanelli & Haynes, 1985; Chung et al., 2009; Zabel et al., 2022). The atomic gas disks of cluster galaxies also have significantly smaller radii than corresponding field galaxies (Giovanelli & Haynes, 1985; Warmels, 1988; Cayatte et al., 1990; Chung et al., 2009). Atomic gas deficiency, def_{HI} , is an estimate of how much the atomic gas content of a cluster has been reduced due to its environment. The def_{HI} definition by Haynes et al. (1984) is widely used in the field (Chung et al., 2009; Zabel et al., 2022), and adopted in this thesis:

$$def_{HI} = \langle \log \bar{\Sigma}_{HI} \rangle - \log \bar{\Sigma}_{HI} \tag{1.3.1}$$

In this equation, $\bar{\Sigma}_{HI} = S_{HI}/D_{opt}^2$, where S_{HI} is the atomic gas flux (Jy km s^{-1}) and D_{opt} is the diameter of the optical disk. $\langle \log \bar{\Sigma}_{HI} \rangle = 0.37$ for all Hubble types (Zabel et al., 2022). def_{HI} shows how much less atomic gas is in a cluster galaxy relative to what is expected from its optical size (Zabel et al., 2022). def_{HI} of galaxies also varies systematically within a cluster. For example, Solanes et al. (2001) found that the def_{HI} of cluster galaxies decreases as we move radially further away from the center of a cluster.

1.3.3 The Virgo Cluster

The Virgo Cluster (Figure 1.2) is a dynamically active and young cluster that is still accreting galaxies (Tully & Shaya, 1984; Yoon et al., 2017; Ferrarese et al., 2012; Zabel et al., 2022). It is the closest galaxy cluster to us, located at 16.5 Mpc (Mei et al., 2007). It has, therefore, been extensively studied in many different wavelengths. Examples of some surveys of the Virgo Cluster are the Röntgen satellite survey (Böhringer et al., 1994) the XMM-Newton, GALEX Ultra-violet Virgo Cluster Survey (Boselli et al., 2011), the Next Generation Virgo Survey (Ferrarese et al., 2012), VLA Imaging of Virgo in Atomic gas (VIVA) (Chung et al., 2009), and Virgo Environment Traced in CO (VERTICO) (Brown et al., 2021). This makes the Virgo Cluster an excellent candidate for spatially resolved studies of the role that environmental mechanisms play in the gas properties of galaxies in the cluster. The mass of the Virgo Cluster is estimated to be $M_{200} = 10^{14.6} M_{\odot}$ (Böhringer et al., 1994; Nulsen & Bohringer, 1995; Girardi et al., 1998; Gavazzi et al., 1999). M_{200} is the total mass within r_{200} of the cluster. r_{200} is the clustercentric radius within which the average mass density is 200 times the critical cosmic density. The r_{200} of the Virgo Cluster is

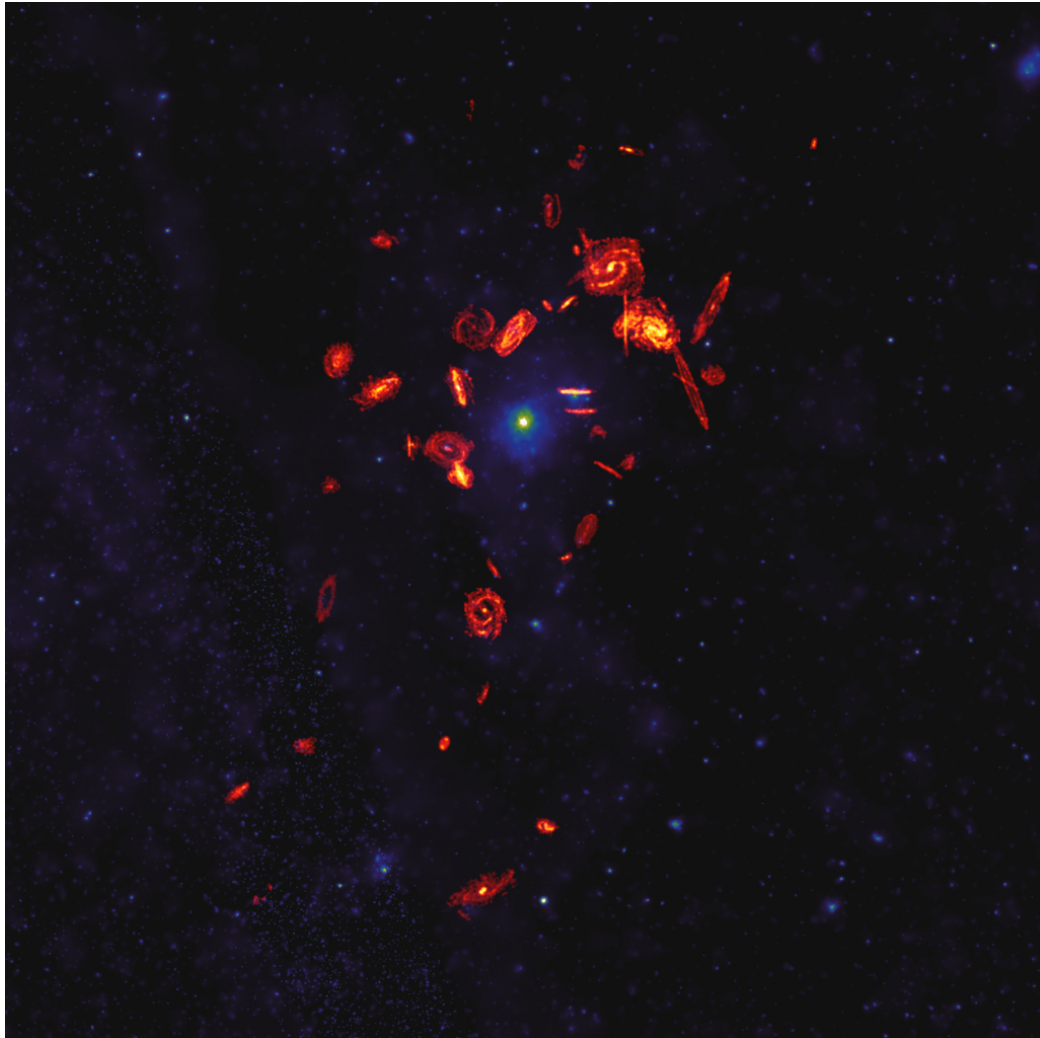


Figure 1.2: Composite image of the Virgo cluster from the VERTICO Survey. Brown et al. (2021) overlaid ALMA radio observations of the molecular gas disk of the galaxies in the VERTICO sample on an X-ray image of the Virgo Cluster plasma. Brown et al. (2021) magnified the radio molecular gas disk images by a factor of 20. Image credit: ALMA (ESO/NAOJ/NRAO)/S. Dagnello (NRAO), Böhringer et al. (1994) (ROSAT All-Sky Survey), Brown et al. (2021) (VERTICO)

estimated to be 1.08-1.55 Mpc (Böhringer et al., 1994; Girardi et al., 1998; Mei et al., 2007; Kim et al., 2014; Boselli et al., 2018).

1.4 The role of pressure in the Interstellar Gas

1.4.1 Turbulent Pressure

In Section 1.1.1 I discussed the significant variation of the velocity dispersion (σ) and surface density (Σ) of molecular clouds. The high variation of these properties implies that the turbulent pressure, which is proportional to $\Sigma\sigma^2$ of molecular clouds, also varies significantly (Sun et al., 2018). Sun et al. (2018) found that turbulent pressure varies across 4 to 5 orders of magnitude. Turbulent pressure plays a key role in balancing out the self-gravity of molecular clouds and preventing them from collapsing (Schinnerer & Leroy, 2024).

Turbulent pressure can play a role in impeding star formation by preventing the molecular gas from reaching the threshold density for star formation (Krumholz et al., 2005; Bigiel et al., 2016; Bemis & Wilson, 2019). However, there has also been some evidence that turbulence can increase star formation (Bemis & Wilson, 2019; Krumholz, 2021). Some magnetohydrodynamic simulations have found turbulent pressure to be the foremost regulator of star formation (Federrath & Klessen, 2012; Kruijssen & Longmore, 2014). Turbulent inflows may be caused by stellar feedback and gas inflows (Krumholz et al., 2018; Bemis & Wilson, 2019; Brunetti et al., 2021).

An extensive amount of research suggests that the mean or ambient pressure in the ISM of a galaxy determines the turbulent pressure in molecular clouds of the galaxy (Keto & Myers, 1986; Elmegreen, 1989; Bertoldi & McKee, 1992; Heyer et al., 2001; Oka et al., 2001; Blitz & Rosolowsky, 2006). This possible relationship is valuable because it links molecular cloud scale properties to large-scale properties of the galaxy that are easier to determine (Sun et al., 2020b). Throughout the literature the terms

mean ISM pressure, ambient ISM pressure, external ISM pressure (P_{ext}), hydrostatic pressure and dynamical equilibrium pressure (P_{DE}) are often used interchangeably, with either slight or no variation in the formalism. I will, therefore, refer to this type of pressure as P_{ext} or P_{DE} to minimize confusion.

More recent works build on the idea that turbulent pressure could be determined by P_{ext} and provide models for the role of P_{ext} in the molecular cloud properties (Field et al., 2011; Hughes et al., 2013b; Johnson et al., 2015; Leroy et al., 2015; Utomo et al., 2015; Meidt, 2016; Schruba et al., 2019; Sun et al., 2020b). Hughes et al. (2013b) explained the differences in σ between giant molecular clouds in M33 and the Large Magellanic Cloud through average ISM pressure. They conclude that the average ISM pressure plays a strong role in determining molecular cloud properties such as σ and Σ . These works are based on the assumption that the molecular clouds exist in an overall state of dynamical equilibrium. This means that the internal pressure of the molecular clouds is balanced with the P_{ext} , the self-gravity of the clouds and the external gravitational potential of the galaxy. Schruba et al. (2019) and Sun et al. (2020b) have found that this is the case.

1.4.2 Dynamical Equilibrium Pressure

In order to calculate P_{ext} , Hughes et al. (2013b) use the hydrostatic pressure formalism from Elmegreen (1989), which is widely used in the field. Assuming the cloud is in hydrostatic equilibrium, the pressure at the boundary of the molecular gas cloud is assumed to be the weight of the layer of interstellar gas. When calculating the weight of this layer of gas we consider the gravitational potential of the total mass of the galaxy that is contained within the layer of gas (Hughes et al., 2013b; Elmegreen,

1989). The Elmegreen (1989) equation for the ambient pressure in the interstellar medium is therefore:

$$P_{ext} = \frac{\pi G}{2} \Sigma_g \Sigma_{total} \quad (1.4.1)$$

Σ_g is the surface density of the interstellar gas layer. This includes both the atomic gas component and the molecular gas component. Σ_{total} is the surface density of the total mass in the layer of gas being considered. We assume that the mass contribution from the dark matter is negligible. The estimate of the total mass surface density is, therefore, $\Sigma_{total} \approx \Sigma_g + (\sigma_g/\sigma_*)\Sigma_*$, where σ_g is the velocity dispersion of the gas, σ_* is the velocity dispersion of the stars, and Σ_* is the stellar surface density (Elmegreen, 1989). This makes the expression for the external ISM pressure to be (Elmegreen, 1989):

$$P_{ext} = \frac{\pi G}{2} \Sigma_g \left(\Sigma_g + \frac{\sigma_g}{\sigma_*} \Sigma_* \right) \quad (1.4.2)$$

Molecular gas is typically found at the midplane of a galaxy (Heyer & Dame, 2015). This expression for P_{ext} is derived from that of the midplane pressure $P_{midplane} = \rho_g \sigma_g^2$, where ρ_g is the density of the gas at the midplane and σ_g is the velocity dispersion of the gas. This general formalism for P_{ext} has been widely adopted across an expansive body of work, some of which are Elmegreen (1989); Elmegreen & Parravano (1994); Wong & Blitz (2002); Blitz & Rosolowsky (2006); Leroy et al. (2008); Koyama & Ostriker (2009); Ostriker & Shetty (2011); Kim et al. (2013); Hughes et al. (2013b); Herrera-Camus et al. (2017); Gallagher et al. (2018); Fisher et al. (2019); Schrubba et al. (2019); Sun et al. (2020b).

Across these works there are only slight variations in the formalism for P_{ext} . For example, Blitz & Rosolowsky (2004); Leroy et al. (2008); Ostriker & Shetty (2011);

Sun et al. (2020b) use this formalism on a kpc scale, which is the same formalism that this thesis uses. They express the density of the total mass in the gas as $\Sigma_{total} \approx \Sigma_{g,kpc} + \sqrt{2G\rho_{\star,kpc}}\sigma_{g,z}$. ρ_{\star} is the midplane stellar volume density, and $\sigma_{g,z}$ is the vertical velocity dispersion of the gas. Sun et al. (2020b) calls this pressure the dynamical equilibrium pressure (P_{DE}), because it is the midplane pressure that arises from dynamical equilibrium. We adopt this term and call this pressure the dynamical equilibrium pressure for the rest of this thesis, with

$$P_{ext} = P_{DE,kpc} = \frac{\pi G}{2}\Sigma_{g,kpc}^2 + \Sigma_{g,kpc}\sqrt{2G\rho_{\star,kpc}}\sigma_{g,z} \quad (1.4.3)$$

In this form the first term is the weight of the gas component of the ISM, and the second term is the weight of the stellar component of the galaxy. For a detailed description of the calculation of the variables for P_{DE} in this thesis refer to Section 2.3.

1.5 This Thesis

1.5.1 Motivation for this Thesis

As discussed in Section 1.1, the breakdown of the cold interstellar gas into the atomic and molecular gas components, which is parameterised by R_{mol} , varies from galaxy to galaxy as well as spatially within galaxies. Understanding this variation of R_{mol} is crucial to the study of galaxy evolution, particularly when considering the framework of gas-centric models of galaxy evolution.

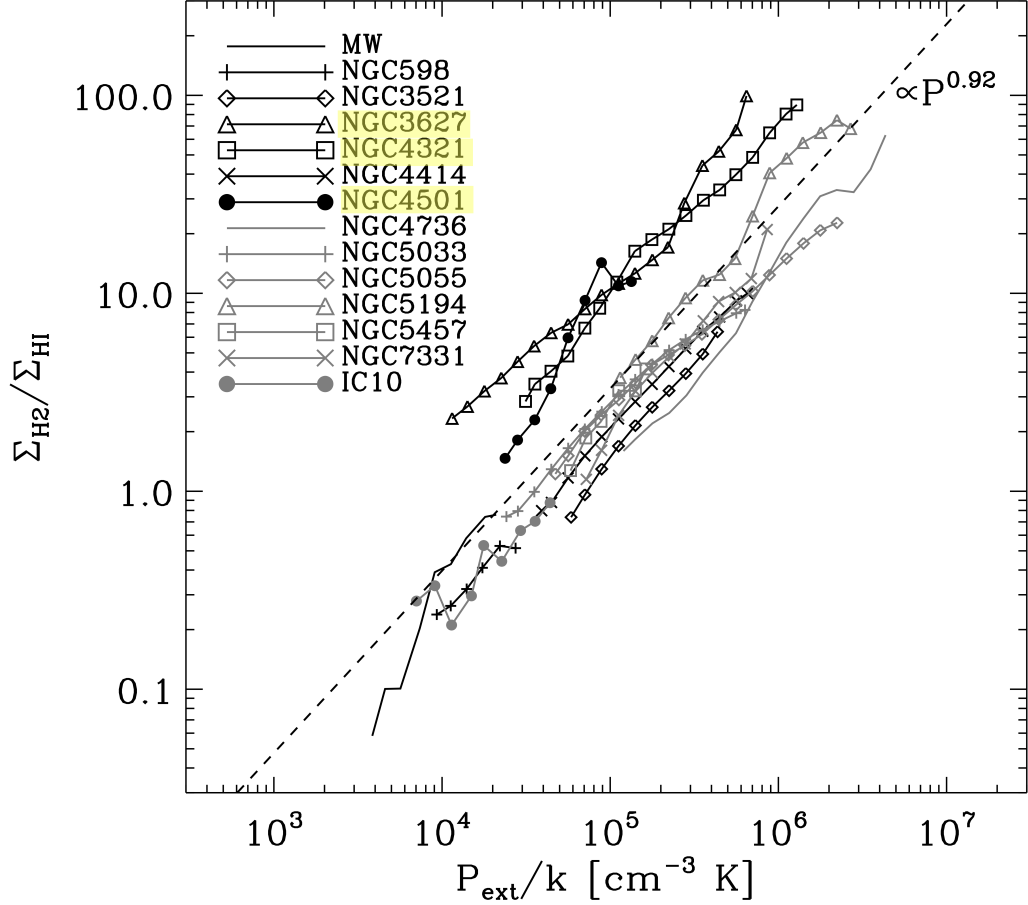


Figure 1.3: Molecular gas ratio (R_{mol}) as a function of dynamical equilibrium pressure for 14 galaxies. The dashed line is the best-fit line, and has a mean index of 0.92 ± 0.07 . Image credit: (Blitz & Rosolowsky, 2006)

Blitz & Rosolowsky (2004) studied 28 galaxies and found that R_{mol} at a specific radius in spiral galaxies could be a function of P_{DE} . Blitz & Rosolowsky (2006) extended this analysis to a wider range of radii and pressure values for 14 galaxies. Their sample of galaxies includes a variety of galaxies such as the Milky Way, dwarf galaxies, HI-rich and H_2 rich galaxies. As shown in Figure 1.3 they found the relationship to hold across 3 orders of magnitude with a root mean scatter of 2 for all galaxies. This relationship between P_{DE} and R_{mol} has subsequently been further

confirmed by other observational studies (Kim & Ostriker, 2007; Leroy et al., 2008; Sun et al., 2020b).

In Figure 1.3 we can see that Blitz & Rosolowsky (2006) found three galaxies out of their 14 galaxy sample to have elevated R_{mol} to P_{DE} values. These offset galaxies are NGC 3627, NGC 4321 and NGC 4501. NGC 3627 is part of the Leo triplet of galaxies and there is evidence that it has recently interacted with NGC 3628. NGC 4321 and 4501 are both members of the Virgo Cluster. These offset galaxies, and our understanding of environmental mechanisms, motivated the hypothesis for this thesis that galaxies in clusters may have systematically higher spatially resolved R_{mol} to P_{DE} values than those of field galaxies.

This thesis also aims to understand the role that the P_{DE} plays in star formation across different galactic environments. The scaling relations explained in Section 1.2, such as the Kennicutt-Schmidt relation and the star-forming main sequence vary based on other factors, such as galaxy morphology and galaxy environment. The variation of these scaling relations could suggest that they do not depict the full physics of star formation (Ellison et al., 2024). The linear relationship between R_{mol} and P_{DE} has led to ‘self-regulating’ models of star formation, which has led to pressure-regulated feedback-modulated models (Ostriker & Shetty, 2011; Shetty & Ostriker, 2012; Kim et al., 2013; Ostriker & Kim, 2022). According to this model the weight of the interstellar medium is balanced by the energy output of massive stars, and it is this balance that determines star formation in a galaxy. According to this model, SFR would be correlated with P_{DE} . This relationship has been empirically confirmed over a range of galaxy morphologies by a number of studies (Herrera-Camus et al., 2017; Fisher et al., 2019; Sun et al., 2020b; Barrera-Ballesteros et al., 2021; Ellison

et al., 2024). Barrera-Ballesteros et al. (2021) argue that, because the Σ_{SFR} vs. P_{DE} relation is consistent over a range of galaxy morphology, and has less scatter than the resolved star-forming main sequence and the resolved Kennicutt-Schmidt relation, P_{DE} could be the fundamental parameter that regulates star formation at kpc scales. Furthermore, Ellison et al. (2024) uses random forest analysis to demonstrate that P_{DE} is a better predictor of star formation than Σ_{\star} or Σ_{H_2} . If R_{mol} vs. P_{DE} varies with environment, it is likely that the role that P_{DE} plays in star formation is also influenced by environment.

1.5.2 Outline for this Thesis

In Chapter 2 I discuss the selection criteria of both my samples of galaxies, the characteristics of the data that I use, and the calculations I perform. This includes the calculation of P_{DE} , as well as the calculations of other galaxy properties, such as def_{HI} . In Chapter 3 I summarize my key results. I demonstrate how R_{mol} , τ_{mol} , and Σ_{SFR} as functions of P_{DE} are different for field galaxies relative to cluster galaxies. I also outline my findings on the impact that environmental mechanisms have on these relationships for cluster galaxies. In Chapter 4 I summarize my main conclusions and discuss the future work I intend to do to follow up this thesis.

Chapter 2

Observational Data and Methods

In order to study the role of environment on P_{DE} in galaxies I compare two samples of galaxies. The first is a sample of field galaxies discussed in section 2.1, and the second is a sample of galaxies in the Virgo Cluster, discussed in Section 2.2. In Section 2.3 I outline how I calculate P_{DE} for the galaxies that I study.

2.1 Field Galaxies Sample

My sample of field galaxies is a sub-sample of the galaxies studied in both the Heterodyne Receiver Array CO Line Extragalactic Survey (HERACLES, Leroy et al. (2009)) and the HI Nearby Galaxy Survey (THINGS, Walter et al., 2008).

The goal of THINGS is to investigate the atomic gas content of galaxies over a wide range of Hubble types. The THINGS sample consists of 34 galaxies with distances of 2-15 Mpc observed with a spatial resolution of 100 to 500 pc. The intentionally diverse galaxy sample contains a broad range of properties with atomic gas masses of $10^7 M_{\odot}$ to $1.4 \times 10^{10} M_{\odot}$, $10^{-3} < \text{SFR} < 6 M_{\odot} \text{ yr}^{-1}$, metallicities ($12 + \log[\text{O}/\text{H}]$)

Table 2.1: Field galaxy sample overview

Galaxy	$\log M_{\star}^a$ (M_{\odot})	$\log \text{SFR}^b$ ($M_{\odot} \text{ yr}^{-1}$)	$\log \text{sSFR}^c$ (yr^{-1})	$\log M_{\text{HI}}^d$ (M_{\odot})	$\log M_{\text{H}_2}^e$ (M_{\odot})	R_{\star}^f (kpc)
NGC 0628	10.24	0.23	-10.01	8.9	9.32	3.38
NGC 2841	10.93	-0.07	-11.00	9.93	8.85	3.59
NGC 3184	10.37	0.13	-10.24	9.49	9.37	3.54
NGC 3351 *	10.28	0.07	-10.21	9.08	9.11	3.42
NGC 3521	10.83	0.42	-10.41	9.9	9.61	3.33
NGC 3627 *	10.67	0.5	-10.17	8.91	9.58	3.39
NGC 4214	8.55	-0.91	-9.46	8.61	6.96	2.82
NGC 4736 *	10.33	-0.33	-10.66	8.6	8.77	3.06
NGC 5055	10.72	0.28	-10.44	9.96	9.61	3.45
NGC 5194 *	10.73	0.65	-10.08	9.4	9.87	3.51
NGC 5457 *	10.39	0.54	-9.85	10.15	9.34	3.62

Notes: ^a Global stellar mass from Leroy et al. (2019) ^b Global star formation rate from Leroy et al. (2019). ^c Global specific star formation rate calculated from column a and column b ^d Global atomic gas mass from Walter et al. (2008). ^e Global molecular gas mass Leroy et al. (2009). ^f Stellar radius estimate from the exponential disk fit in Salo et al. (2015) * Galaxies that are in groups (M96 group, Leo triplet, M94 group, M51 group, M101 Group)

of 7.5 to 9.2, and absolute luminosities M_B of -11.5 mag to -21.7 mag (Walter et al., 2008).

HERACLES was designed to complement the HI maps of galaxies produced by THINGS with CO maps of the galaxies. Initially, HERACLES produced CO(2-1) maps for 18 galaxies, using the IRAM 30-meter telescope (Leroy et al., 2009). The sample of HERACLES was then expanded to include 33 galaxies in Schrubba et al. (2011) This thesis uses the HERACLES sample outlined in Brown et al. (2021). From a further updated HERACLES sample of 48 galaxies. Brown et al. (2021) excluded 18 galaxies that were non-detections and 5 galaxies that overlapped with the VERTICO sample to produce a HERACLES comparison sample of 25 galaxies. The distances of the galaxies in this HERACLES sample range from 2 Mpc to 25

Mpc. The stellar mass range of the sample is $10^{8.5}$ to $10^{11} M_{\odot}$ and the specific star formation (sSFR=SFR/ M_{\star}) rate range is $10^{-11.5} < \text{sSFR} < 10^{-9.2} M_{\odot} \text{ yr}^{-1}$ (Brown et al., 2021). Brown et al. (2021) smoothed both the atomic and molecular data of the sample to a physical resolution of 1.2 kpc. I then apply a maximum inclination cut of 70° to the 23 galaxies available in the VERTICO SQL database, which reduces the sample size to 20 galaxies. I apply this widely used inclination cut because I cannot accurately perform my calculations on edge-on galaxies. I also apply a minimum signal-to-noise ratio cut of 2 to the molecular gas mass surface density. This does not further exclude any galaxies from the sample. I then apply a minimum value cut of $10^{-7} M_{\odot} \text{ pc}^{-2}$ to the atomic gas mass surface density values of the pixels. This reduces the galaxy sample to 13. From this sample I only select galaxies for which the fits to measure stellar radius are available from Salo et al. (2015), which further reduces my sample size to 11. More details on the stellar radius fits that I use for the P_{DE} calculation are given in Section 2.3. After these cuts, the resulting field galaxy sample that I use for this thesis is outlined in Table 2.1. The field galaxy sample has a stellar mass range of $10^{8.55}$ to $10^{10.93} M_{\odot}$ and a star formation rate range of 0.12 to $4.47 M_{\odot} \text{ yr}^{-1}$.

2.2 Cluster Galaxies Sample

The sample of cluster galaxies that I use in this thesis are 30 galaxies in the Virgo Cluster that are studied in both the VERTICO survey (Brown et al., 2021) and the VIVA survey (Chung et al., 2009) with a few additional selection criteria. VIVA produced high-resolution HI maps for 53 galaxies in the Virgo cluster, using the C short configuration of the VLA. The VIVA sample was selected to be representative

of the types of galaxies in the Virgo cluster. The VERTICO Survey observed the CO J=2-1 line for 51 out of the 53 galaxies in the VIVA sample, using the Atacama Compact Array, which is a part of ALMA.

Galaxies in the Virgo cluster experience a wide range of environmental effects (Zabel et al., 2022). The VIVA sample consists of 48 spiral galaxies and 5 irregular galaxies. 60% of the galaxies in the VIVA sample are fainter than $B_T > 12$ mag. This is different from samples in previous studies of the Virgo Cluster that were biased towards brighter galaxies (Chung et al., 2009). Faint galaxies that have high B_T values tend to be more vulnerable to the environmental effects of a cluster (Chung et al., 2009), and are, therefore, important to include in the sample. The VIVA sample consists of galaxies from regions with a wide range of densities in Virgo. The galaxy M87 is considered to be the center of the Virgo Cluster. VIVA, therefore, studies galaxies within 0.3 to 3.3 Mpc from the M87 (Chung et al., 2009). This is equivalent to up to 4 virial radii of the Virgo Cluster (Tully & Shaya, 1984).

The VIVA sample was also designed to encompass galaxies with a range of star formation properties. They used the results of Koopmann & Kenney (2004) who classified 84 galaxies in the Virgo Cluster into star formation property categories using H_α and R-band observations. These categories are truncated, enhanced, anemic and normal. According to Koopmann & Kenney (2004) the different star formation property categories reflect the different environmental mechanisms that galaxies in the Virgo Cluster experience, as well as their different evolutionary stages. The VIVA Survey, therefore, selected 46 galaxies across all of Koopmann & Kenney (2004)’s star formation categories in the Virgo cluster.

The VIVA sample also contains galaxies that are not part of the Koopmann &

Kenney (2004) survey. IC 3418 and NGC 4330 are members of the VIVA sample that were selected from the GALEX survey (Martin & GALEX Team, 2005), because they displayed unique morphological characteristics in the UV image. NGC 4216, IC 3355, NGC 4533, VCC 1581 and VCC 2062 are galaxies in the VIVA sample that are also not part of the Koopmann & Kenney (2004) survey. These galaxies were included because they were spatially close to one of the target galaxies, and could, therefore, be observed simultaneously with the VLA. As a result of this careful selection process the VIVA sample consists of 53 galaxies that together are representative of the Virgo Cluster late-type galaxy population in terms of morphology, subcluster membership, HI mass, HI deficiency and systemic velocity (Chung et al., 2009).

The VERTICO Survey observed CO maps for 51 out of the 53 galaxies in VIVA. IC 3355 and VCC 2062 are part of the VIVA sample, but were excluded from the VERTICO sample, because their low masses make them difficult to detect with CO emission (Brown et al., 2021). Of these 51 galaxies, 49 were detected and mapped in the CO J=2-1 line. I apply the same selection criteria to this cluster sample that I did to the field sample. I apply a maximum inclination cut of 70° which reduces the sample size from 49 galaxies to 34 galaxies. I also apply a minimum signal-to-noise ratio cut of 2 to the molecular gas mass surface density. This does not further exclude any galaxies from the sample. I also only select galaxies for which the appropriate stellar radius is available from Salo et al. (2015), which eliminates 4 galaxies. I, therefore, end up with a sample of 30 galaxies in the Virgo Cluster that are listed in Table 2.2

The cluster sample used in this thesis has a global stellar mass range of $10^{9.06}$ to $10^{11} M_\odot$, and a global star formation rate range of 0.123 to $4.47 M_\odot \text{ yr}^{-1}$. As can be

Table 2.2: Cluster galaxy sample overview

Galaxy	$\log M_{\star}^a$ (M_{\odot})	$\log \text{SFR}^b$ ($M_{\odot} \text{ yr}^{-1}$)	$\log \text{sSFR}^c$ (yr^{-1})	$\log M_{\text{HI}}^d$ (M_{\odot})	$\log M_{\text{H}_2}^e$ (M_{\odot})	R_{\star}^f (kpc)
IC 3392	9.51	-1.3	-10.81	7.66	8.37	3.0
NGC 4064	9.47	-1.07	-10.54	7.63	8.41	3.15
NGC 4189	9.75	-0.33	-10.08	8.78	8.69	3.18
NGC 4254	10.52	0.7	-9.82	9.72	9.88	3.4
NGC 4298	10.11	-0.26	-10.37	8.72	9.08	3.27
NGC 4299	9.06	-0.34	-9.40	9.07	7.58	3.02
NGC 4321	10.71	0.54	-10.17	9.49	9.84	3.63
NGC 4351	9.37	-0.91	-10.28	8.5	7.85	3.07
NGC 4380	10.11	-0.77	-10.88	8.13	8.59	3.27
NGC 4383	9.44	0.01	-9.43	9.49	8.37	2.72
NGC 4394	10.34	-0.79	-11.13	8.67	7.98	3.19
NGC 4405	9.75	-0.88	-10.63	7.68	8.27	2.91
NGC 4424	9.89	-0.52	-10.41	8.29	8.31	3.19
NGC 4450	10.7	-0.55	-11.25	8.48	8.67	3.38
NGC 4457	10.42	-0.49	-10.91	8.31	9.02	3.03
NGC 4501	11.0	0.43	-10.57	9.25	9.69	3.4
NGC 4532	9.25	-0.16	-9.41	9.32	8.25	3.04
NGC 4535	10.49	0.31	-10.18	9.54	9.41	3.55
NGC 4548	10.65	-0.28	-10.93	8.83	8.99	3.44
NGC 4561	9.09	-0.64	-9.73	9.17	7.31	2.96
NGC 4568	10.47	0.29	-10.18	9.21	9.41	3.25
NGC 4569	10.86	0.16	-10.70	8.82	9.58	3.5
NGC 4579	10.92	0.08	-10.84	8.78	9.31	3.37
NGC 4580	9.94	-0.9	-10.84	7.47	8.55	3.08
NGC 4651	10.31	-0.1	-10.41	9.63	8.76	3.12
NGC 4654	10.26	0.31	-9.95	9.5	9.33	3.38
NGC 4689	10.16	-0.29	-10.45	8.7	9.02	3.41
NGC 4698	10.49	-0.83	-11.32	9.24	7.94	3.17
NGC 4713	9.31	-0.2	-9.51	9.49	8.38	3.1
NGC 4772	10.18	-1.08	-11.26	8.95	7.4	3.17

Notes: ^a Global stellar mass from Leroy et al. (2019) ^b Global star formation rate from Leroy et al. (2019). ^c Global specific star formation rate calculated from column a and column b ^d Global atomic gas mass from Walter et al. (2008). ^e Global molecular gas mass Leroy et al. (2009). ^f Stellar radius estimate from the exponential disk fit in Salo et al. (2015)

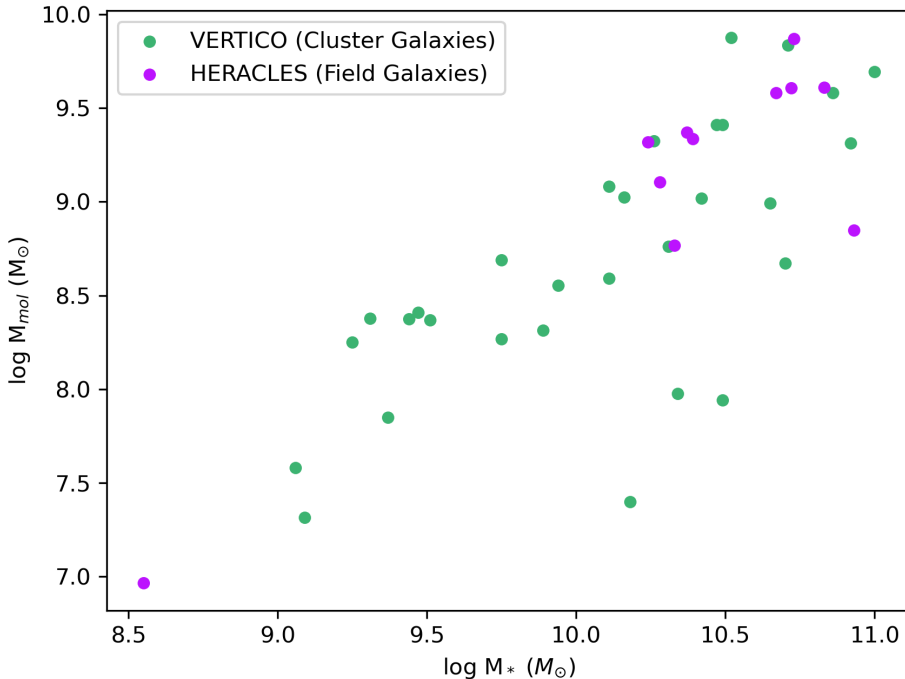


Figure 2.1: The global molecular gas mass estimates vs. the global stellar mass estimates of the galaxies in both samples. The purple data points represent the galaxies in the cluster sample, and the green data points represent the galaxies in the field sample.

seen in Figures 2.1 and 2.2, the field galaxy sample and cluster galaxy sample have different distributions of global stellar mass, molecular gas mass, and star formation rates. The field galaxy sample has one galaxy, NGC 4214, with a significantly lower mass and star formation rate than any of the other galaxies in the field sample or the galaxies in the cluster sample. I have chosen to include this galaxy in my thesis, despite this causing the global ranges of the samples to be different because low-mass galaxies are often most susceptible to the effects of the environment. I also explore the effect of only including galaxies with global $M_* > 10^{10}$ for both samples. A detailed discussion on the significance of this range cut is given in Section 3.4.

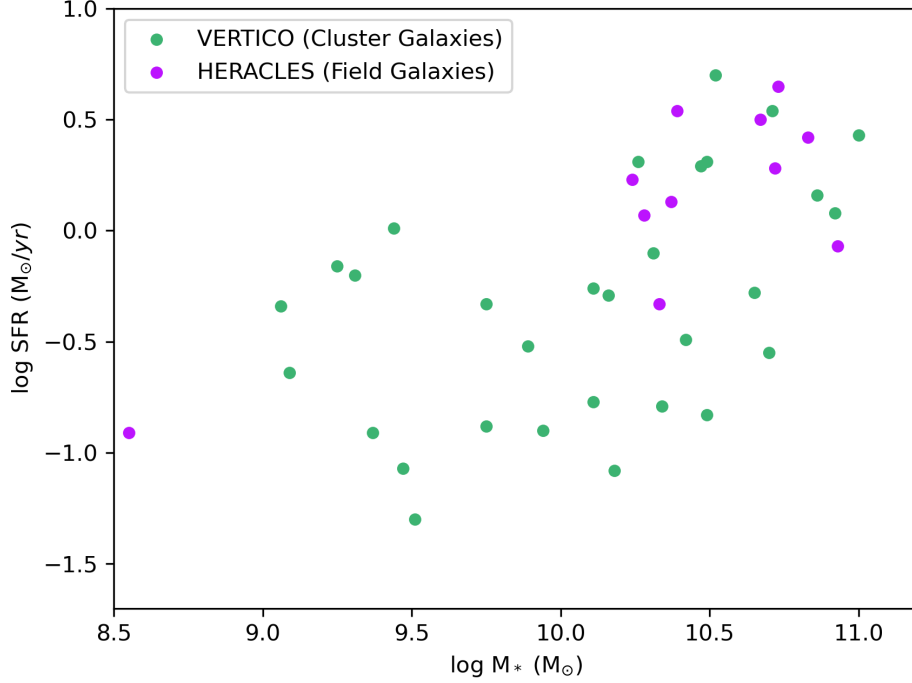


Figure 2.2: The global star formation rate estimates vs. the global stellar mass estimates of the galaxies in both samples. The purple data points represent the galaxies in the cluster sample, and the green data points represent the values in the field sample.

2.3 Dynamical Equilibrium Pressure Calculation

For my calculation of P_{DE} I apply the dynamical equilibrium calculation below to 1.2 kpc scale data,

$$P_{ext} = P_{DE,kpc} = \frac{\pi G}{2} \Sigma_{g,kpc}^2 + \Sigma_{g,kpc} \sqrt{2G\rho_{*,kpc}} \sigma_{g,z} \quad (2.3.1)$$

To calculate the Σ_g values in equation 2.3.1 I added together the atomic gas mass surface density map (Σ_{HI}) and the molecular gas mass surface density map (Σ_{mol}) for every galaxy. For details on the 1.2 kpc atomic gas and molecular gas mass moment

0 maps used, refer to Brown et al. (2021) and Leroy et al. (2009). Brown et al. (2021) and Leroy et al. (2009) calculated the molecular gas masses from the CO (J=2-1) line intensity (I_{CO}) in units of K km/s using :

$$\Sigma_{mol} = \frac{\alpha_{co}}{R_{21}} I_{CO} \quad (2.3.2)$$

where $R_{21} = 0.8$, and $\alpha_{CO} = 4.35 M_{\odot} \text{ pc}^{-2} (\text{K km s}^{-1})^{-1}$ (Bolatto et al., 2013; Brown et al., 2021). Brown et al. (2021) smoothed the higher resolution CO data to the 1.2 kpc linear resolution ($15''$ angular resolution) of the HI data.

In order to calculate the midplane stellar volume density, ρ_{star} (M_{\odot}/pc^3), I adopt the estimation used by Blitz & Rosolowsky (2006); Leroy et al. (2008); Ostriker & Shetty (2011); Sun et al. (2020b):

$$\rho_{\star} = \frac{\Sigma_{\star}}{4H_{\star}} = \frac{\Sigma_{\star}}{0.54R_{\star}} \quad (2.3.3)$$

where Σ_{\star} (M_{\star}/pc^2) is the stellar surface mass density, H_{\star} (pc) is the scale height of the stellar disk and $H_{\star} = 0.135R_{\star}$. R_{\star} (pc) is the scale radius of the stellar disk.

In order to produce the 1.2 kpc scale Σ_{\star} maps Brown et al. (2023) used infrared images by Wide-field Infrared Survey Explorer (WISE). The WISE images at wavelengths $3.4 \mu m$, $4.6 \mu m$, $12 \mu m$, and $22 \mu m$ are referred to as WISE1, WISE2, WISE3 and WISE4 respectively (Leroy et al., 2019). Brown et al. (2023) calculated the Σ_{\star} maps by applying local mass-to-light ratios (Υ_{\star}) to WISE-1 photometric observations ($I_{3.4\mu m}$) according to the methodology from Leroy et al. (2019):

$$\frac{\Sigma_{\star}}{M_{\odot} \text{ pc}^2} \approx 3.3 \times 10^2 \left(\frac{\Upsilon_{\star}}{0.5} \right) \left(\frac{I_{3.4\mu m}}{\text{MJy sr}^{-1}} \right) \quad (2.3.4)$$

Brown et al. (2023) calculated spatially resolved mass-to-light ratios using the WISE3-WISE1 colour (Leroy et al., 2019)

$$\Upsilon_{\star}[M_{\odot}L_{\odot}^{-1}] = \begin{cases} 0.5, & \text{if } Q < a \\ 0.5 + b(Q-a), & \text{if } a < Q < c \\ 0.2, & \text{if } Q > c \end{cases} \quad (2.3.5)$$

where Q is $\log(L_{\text{WISE3}}/L_{\text{WISE1}})$, a is 0.1, b is -0.46 and c is 0.75.

For estimates of the R_{\star} values of the galaxies in my sample, I used the results of the Spitzer Survey of Stellar Structure in Galaxies (S⁴G, Sheth et al., 2008) in Salo et al. (2015). As part of this survey Salo et al. (2015) conducted deep imaging of galaxies in wavelengths 3.6 μm and 4.5 μm . Salo et al. (2015) used GALFIT3.0 to decompose the 3.6 μm surface brightness profiles of the galaxies with a variety of models. I use the R_{\star} estimates produced by their two-component model. For this model the bulge component of the galaxy is modelled using a Sérsic profile (Salo et al., 2015)

$$\Sigma(r) = \Sigma_e \exp(-\kappa[(r/R_e)^{1/n} - 1]) \quad (2.3.6)$$

where Σ_e is the surface brightness at the isophotal radius that encompasses half of the total flux of the bulge component, κ is a normalization constant and n is the Sérsic index. $n=1$ corresponds to an exponential curve, and $n=4$ corresponds to a de Vaucouleurs profile. The disk component of the galaxy is modeled as an infinitesimally thin exponential disk:

$$\Sigma(r) = \Sigma_o q^{-1} \exp(-r/R_\star) \quad (2.3.7)$$

where $\Sigma(r)$ is the modelled surface brightness of the disk component, Σ_o is the peak surface brightness of the disk at the centre, q is the inclination correction $\cos(i)$, and r is the radial coordinate.

For the P_{DE} calculation, $\sigma_{g,z}$ is the mass-weighted sum of the average vertical velocity dispersion of the atomic gas component (σ_{HI}) and the average vertical velocity dispersion of the molecular gas component (σ_{mol}) (Sun et al., 2020b),

$$\sigma_{g,z} = f_{mol} \langle \sigma_{mol} \rangle + (1 - f_{mol}) \langle \sigma_{HI} \rangle \quad (2.3.8)$$

where $f_{mol} = \Sigma_{mol}/(\Sigma_{HI} + \Sigma_{mol})$ is the fraction of the molecular gas mass over the total gas mass which I calculate from gas mass surface densities. Instead of using the moment 2 maps of atomic gas and molecular gas for the values of σ_{HI} and σ_{mol} , I use constant values. This is because the moment 2 maps include movement in both the vertical and radial directions, as well as a component due to the galaxy's rotation velocity. The moment 2 maps would, therefore, overestimate the σ_{HI} and σ_{mol} values.

Multiple works measure constant values for the gas vertical velocity dispersion values (Leroy et al., 2008; Tamburro et al., 2009; Wilson et al., 2011; Caldú-Primo et al., 2013; Mogotsi et al., 2016). Walter et al. (2008) found the average σ_{HI} to be $11 \pm 3 \text{ km s}^{-1}$ over the radius range $r_{25}/2 < r < r_{25}$, for the galaxies studied in THINGS, where r_{25} is the radius at which the surface brightness of a galaxy in the B band is $25 \text{ mag arcsec}^{-2}$ (Carroll & Ostlie, 2017). Tamburro et al. (2009) found the

typical σ_{HI} to be $10 \pm 2 \text{ km s}^{-1}$ at r_{25} . For my work I, therefore, assume $\sigma_{HI}=10 \text{ km s}^{-1}$.

While the average molecular gas velocity dispersion for galaxies is expected to be lower than that of the atomic gas, it is not as well constrained (Stark & Brand, 1989; Wilson & Scoville, 1990; Combes & Becquaert, 1997). For my thesis I assume a constant value of 5 km s^{-1} for the molecular gas vertical velocity dispersion. Wilson & Scoville (1990) measured a vertical velocity dispersion of $5 \pm 1 \text{ km s}^{-1}$ for M33. The vertical velocity dispersion is sometimes referred to as the cloud-cloud velocity dispersion in past works. Combes & Becquaert (1997) measured an average velocity dispersion of 6 km s^{-1} for NGC 628, and an average velocity dispersion of 8.5 km s^{-1} for NGC 3938. However, Wilson et al. (2011) argue that the dispersion estimates from Combes & Becquaert (1997) are overestimates, because they do not correct for the internal velocities of giant molecular clouds (GMCs). Wilson et al. (2011) used CO maps from the James Clerk Maxwell Telescope to study σ_{H_2} for 12 spiral galaxies. They found that the molecular gas dispersion is typically half that of atomic gas dispersion value for a galaxy. They found σ_{H_2} to be $6.1 \pm 1.0 \text{ km s}^{-1}$ for their sample.

2.4 Dynamical Equilibrium Pressure vs. a Proxy for Pressure

Watts et al. (2023) used a proxy for P_{DE} , which is a simplified version of the second term of equation 2.3.1,

$$P_p = \Sigma_{\star}^{0.5} \Sigma_g \tag{2.4.1}$$

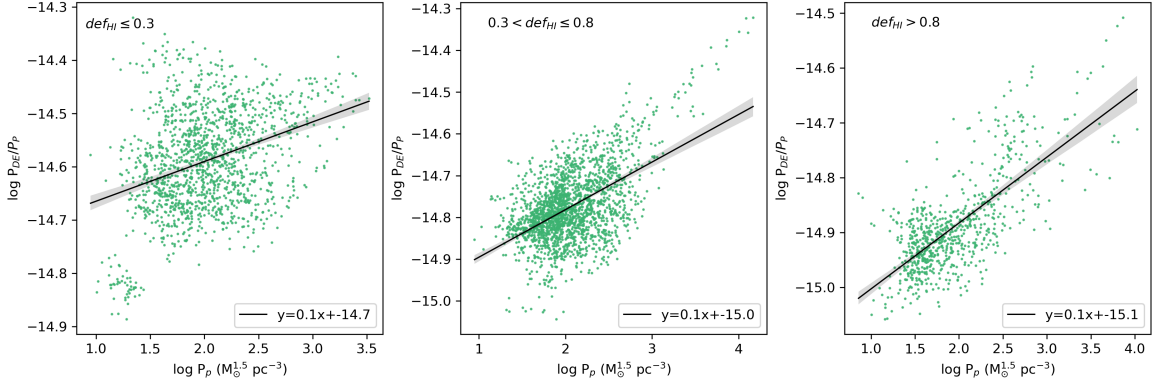


Figure 2.3: A comparison of the P_{DE} values calculated in this thesis with the proxy for pressure used by Watts et al. (2023) equation across atomic gas deficiencies for galaxies in the cluster sample.

They assumed that because Σ_{\star} and Σ_g are the dominant terms, the other terms in equation 2.3.1 are insignificant. In order to examine if it is valuable to calculate the full P_{DE} I examine the relationship of P_{DE}/P_p as a function of P_p . As can be seen in Figure 2.3, not only does the relationship have a very high level of scatter it also shifts based on external factors, such as def_{HI} . Because this thesis is interested in the effect of environmental mechanisms, which is often represented by def_{HI} , I concluded that it is valuable to calculate the full P_{DE} values, instead of only the P_p values.

2.5 Other Properties

For my calculation of R_{mol} at 1.2 kpc scales I divide the 1.2 kpc maps of Σ_{mol} by Σ_{H1} from Brown et al. (2021). For the star formation rates (Σ_{SFR}) I use the 1.2 kpc maps produced by Brown et al. (2023). In order to estimate the star-formation rates of the galaxies Brown et al. (2023) used the 231 nm wavelength Galaxy Evolution Explorer (GALEX) images (I_{NUV}) and WISE3 images (I_{WISE3}), using this calibration from

Leroy et al. (2019):

$$\frac{\Sigma_{SFR}}{M_{\odot}\text{yr}^{-1}\text{kpc}^{-2}} = \left(8.9 \times 10^{-2} \frac{I_{NUV}}{\text{MJy sr}^{-1}} + 4.1 \times 10^{-3} \frac{I_{WISE3}}{\text{MJy sr}^{-1}} \right) \cos i \quad (2.5.1)$$

Using only ultraviolet images to estimate the star formation rates would lead to underestimates of the star formation rate. This is because UV measurements miss the young stellar populations obscured by dust (Leroy et al., 2019). Brown et al. (2023) use the WISE3 images in the SFR calculations because the WISE3 images have higher spatial resolutions of 9" than the WISE4 images (Leroy et al., 2019).

In order to study the impact of the atomic gas stripping that the cluster galaxies experience I use the def_{HI} values for galaxies in the Virgo cluster calculated by Chung et al. (2009), using equation 1.3.1. These values were also adopted by Zabel et al. (2022).

The efficiency of star formation in galaxies is also an important area of study for galaxy evolution. To study how efficiently molecular gas is converted to stars in every galaxy I calculate 1.2 kpc maps of molecular gas depletion time, τ_{mol} , which is equal to $\Sigma_{mol}/\Sigma_{SFR}$.

Chapter 3

Results

One of the aims of my thesis is to understand how the empirically confirmed relationship of R_{mol} as a function of P_{DE} (Blitz & Rosolowsky, 2006; Kim & Ostriker, 2007) varies with galaxy environment. In Section 3.1 I demonstrate the difference in R_{mol} vs. P_{DE} values for cluster galaxies compared to those of field galaxies. I also explore the effect of environmental mechanisms on this difference in this section. The other aim of my thesis is to explore the impact of the environment on pressure-regulated feedback models of star formation. I do this by demonstrating the impact of environment on SFR vs. P_{DE} in Section 3.2, and τ_{mol} vs. P_{DE} in Section 3.3.

3.1 Molecular to Atomic Gas Ratio vs. Dynamical Equilibrium Pressure

Figure 3.1 illustrates that a lot of the cluster galaxy data points have higher R_{mol} at given P_{DE} than the field galaxy data points. The best-fit lines of the cluster galaxy

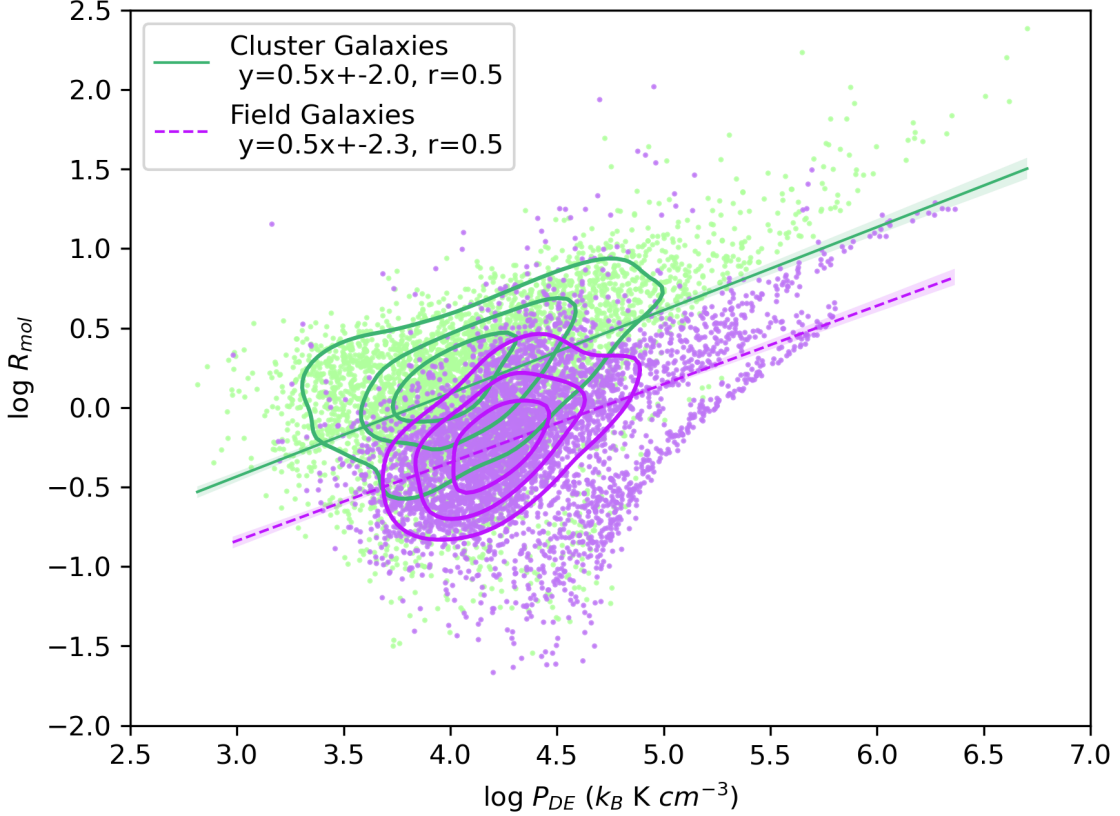


Figure 3.1: Molecular gas ratios (R_{mol}) as a function of dynamical equilibrium pressure (P_{DE}) at 1.2kpc resolution for the field galaxies in purple and the cluster galaxies in green. The field galaxy sample is a sub-sample of the HERACLES survey (Leroy et al., 2009; Brown et al., 2021). The cluster sample is a sub-sample of the VERTICO survey (Brown et al., 2021). The green line is the best-fit line for the R_{mol} vs. P_{DE} data of the cluster galaxy sample, obtained using linear regression. The purple line is the corresponding best-fit line for the field galaxy sample data. The contour lines enclose 25%, 50%, and 75% of the corresponding data points.

sample and field galaxy sample have the same gradient of 0.5, but the cluster galaxy sample best-fit line is shifted towards higher R_{mol} values by 0.3 in log space. This is in agreement with my initial hypothesis discussed in Section 1.5.1 that the cluster galaxies would have higher R_{mol} at given P_{DE} values than the field galaxies.

The mean gas values can be used for an approximate interpretation of the shift

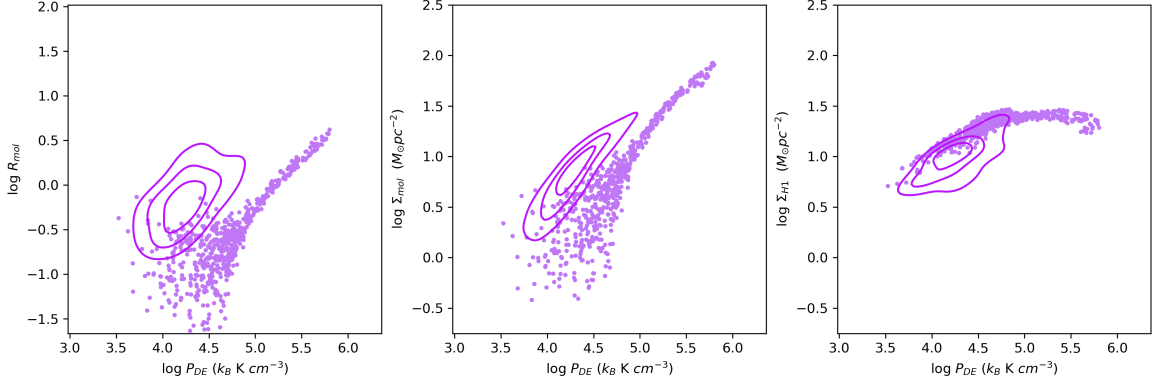


Figure 3.2: Left: The contour lines enclose 25%, 50%, and 75% of the R_{mol} vs. P_{DE} data points of the entire field sample of this thesis. The data points are the individual pixel values of NGC 3521. Middle: The contour lines represent Σ_{mol} vs. P_{DE} data of the entire field sample. The data points are the individual pixel values of NGC 3521. Right: The contour lines represent Σ_{HI} vs. P_{DE} data of the entire field sample of this thesis. The data points are the individual pixel values of NGC 3521.

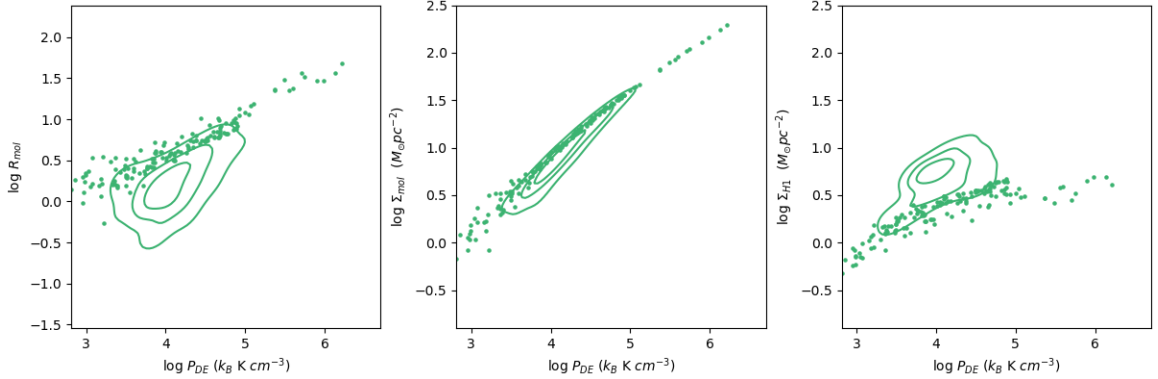


Figure 3.3: Left: The contour lines enclose 25%, 50%, and 75% of the R_{mol} vs. P_{DE} data points of the entire cluster sample. The data points are the individual pixel values of NGC 4569. Middle: The contour lines represent Σ_{mol} vs. P_{DE} data of the entire cluster sample. The data points are the pixel values of NGC 4569. Right: The contour lines represent Σ_{HI} vs. P_{DE} data of the entire cluster sample. The data points are the 1.2 kpc pixel values of NGC 4569.

of the best-fit line between the two samples in Figure 3.1. The mean molecular gas and atomic gas surface densities of the cluster galaxy sample are $11.7 M_{\odot} \text{ pc}^{-2}$ and $5.3 M_{\odot} \text{ pc}^{-2}$. The mean molecular gas and atomic gas surface densities of the field

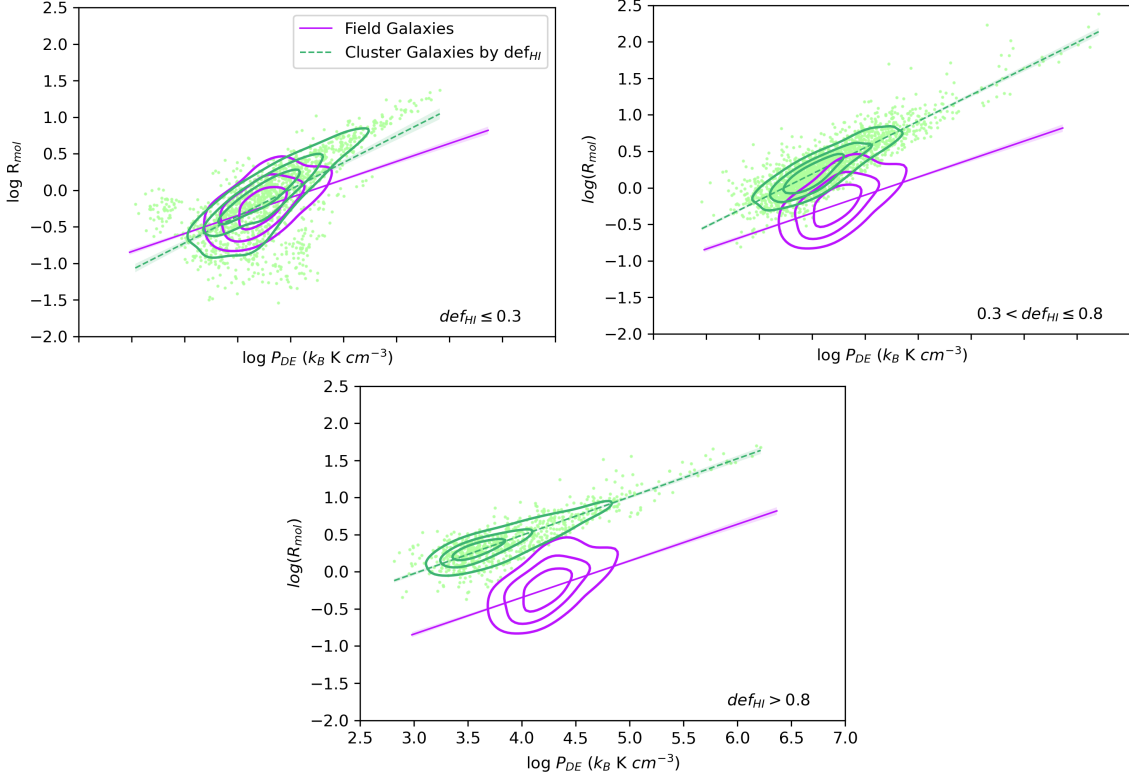


Figure 3.4: The purple contour lines and the purple best-fit line in all the panels correspond to the R_{mol} vs. P_{DE} values of the field sample of this thesis and are the same as those in Figure 3.1. The equation of the best-fit line of the field sample is $y = 0.5x - 2.3$. Top-left: The green data points, contour lines and best-fit line represent the R_{mol} vs. P_{DE} values of the sub-sample of cluster galaxies that have atomic gas deficiencies ≤ 0.3 . The green best-fit line equation is $y = 0.7x - 3.3$. Top-right: The green data points, contour lines and best-fit line represent the R_{mol} vs. P_{DE} values of the sub-sample of cluster galaxies that have atomic gas deficiency values between 0.3 to 0.8. The green best-fit line equation is $y = 0.7x - 2.7$. Bottom: The green data points, contour lines and best-fit line represent the R_{mol} vs. P_{DE} values of the sub-sample of cluster galaxies that have atomic gas deficiency values greater than 0.8. The green best-fit line equation is $y = 0.5x - 1.6$.

galaxy sample are $12.1 M_{\odot} \text{ pc}^{-2}$ and $10.7 M_{\odot} \text{ pc}^{-2}$. In order for a change in P_{DE} to exclusively account for the shift of the best-fit line, P_{DE} would have to decrease by a factor ~ 4 from the field sample to the cluster sample. The mean value of Σ_g of the cluster sample is lower than that of the field sample by a factor of 1.34. Even if the Σ_g^2 term was the dominant term in the P_{DE} equation 2.3.1, this would cause the mean P_{DE} value to increase by a factor of ~ 1.8 . Meanwhile, for R_{mol} to exclusively account for the shift of the best-fit line, R_{mol} would have to increase by a factor ~ 2 from the field to the cluster sample. The mean R_{mol} values of the samples differ by a factor of ~ 2 . This could mean that a change in R_{mol} , as opposed to a change in P_{DE} is the primary cause of the difference between the 2 samples. However, mean values are not sufficient information for a conclusive picture of the driving forces behind the shift in Figure 3.1.

Both samples in Figure 3.1 have a high level of scatter. To understand the source of this scatter, I examined some individual galaxies. NGC 3521 is a field galaxy with some of the lowest R_{mol} values in the field sample. This is illustrated in the left-hand panel of Figure 3.2. The middle panel of Figure 3.2 illustrates that there is quite a large vertical spread of Σ_{mol} values, despite NGC 3521 containing relatively high P_{DE} values. The right panel of Figure 3.2 demonstrates that the majority of the Σ_{HI} vs. P_{DE} data points of NGC 3521 are higher than those of the rest of the galaxies in the field sample. Because $R_{mol} = \Sigma_{mol}/\Sigma_{HI}$, this combination of low Σ_{mol} and high Σ_{HI} explains why the R_{mol} vs. P_{DE} relation is shifted downwards for NGC 3521 relative to the field sample as a whole.

Figure 3.3 shows the gas content of the cluster galaxy NGC 4569 that has high R_{mol} vs. P_{DE} values relative to the rest of the cluster sample. NGC 4569 is a cluster

galaxy that is extremely HI deficient ($\text{def}_{HI} = 1.47 \pm 0.2$) and has a Yoon et al. (2017) classification of 3 (Zabel et al., 2022). Galaxies with a Yoon et al. (2017) classification of 3 have severely truncated HI disks and are extremely HI deficient. NGC 4569, therefore, has low HI values relative to the rest of the cluster sample as reflected in the right panel of Figure 3.3. The left panel of Figure 3.3 demonstrates the relatively high R_{mol} vs. P_{DE} values of NGC 4569, as well as the relatively tight correlation between the two quantities for NGC 4569. The middle panel of Figure 3.3 shows the relatively high Σ_{mol} vs. P_{DE} values of NGC 4569. This explains the relatively high R_{mol} vs. P_{DE} values of NGC 4569 in the left panel of Figure 3.3.

Individual galaxies in both the field and cluster samples have relatively tight correlations between R_{mol} and P_{DE} . The individual relations of every galaxy can be seen in Figures A.1 and A.2 in the Appendix A. My examination of the gas content of galaxies with significantly high or low R_{mol} values relative to the rest of the sample revealed that they also had significantly skewed gas content. I, therefore, conclude that the high scatter of each sample is significantly driven by the large variation of gas content from galaxy to galaxy within each sample.

A possible reason for the relatively elevated R_{mol} vs. P_{DE} values of the cluster galaxy sample is the atomic gas stripping that cluster galaxies experience due to environmental mechanisms (Haynes et al., 1984; Verheijen & Sancisi, 2001; Zabel et al., 2022). Atomic gas is the most susceptible to environmental stripping because it is typically the most extended component of the interstellar medium (Cayatte et al., 1990). To investigate the role of atomic gas stripping, I split up my cluster galaxy sample into three def_{HI} bins: $\text{def}_{HI} \leq 0.3$, $0.3 < \text{def}_{HI} \leq 0.8$, and $\text{def}_{HI} > 0.8$. I adopted these bin values from Zabel et al. (2022). The def_{HI} values I use are

calculated by Chung et al. (2009).

Figure 3.4 illustrates the significant role that def_{HI} plays in the relatively higher R_{mol} vs. P_{DE} values of the cluster sample compare to those of the field sample. The top left panel of Figure 3.4 illustrates that when comparing cluster galaxies with low def_{HI} values to my full field sample, the observed difference in R_{mol} vs. P_{DE} of the two samples reduces significantly. The best-fit line of the $\text{def}_{HI} \leq 0.3$ cluster galaxy sample is $y = 0.7x - 3.3$. The contours of the samples overlap far more than in Figure 3.1. The top right panel of Figure 3.4 compares cluster galaxies with medium def_{HI} values to the full field galaxy sample. The best-fit line of the cluster sub-sample shifts upwards to $y = 0.7x - 2.7$. The bottom panel of Figure 3.4 compares cluster galaxies with $\text{def}_{HI} \geq 0.8$ with the full field sample. This bottom panel has the largest difference between the field sample and cluster sub-sample. The best-fit line for the cluster galaxy sub-sample with $\text{def}_{HI} \geq 0.8$ is $y = 0.5x - 1.6$. Figure 3.4 demonstrates a steady shift of the best-fit line from lower to higher R_{mol} at a given P_{DE} with increasing def_{HI} . Figure 3.4, therefore, illustrates that the galaxies with higher def_{HI} , which experience more atomic gas stripping, drive the difference in R_{mol} vs. P_{DE} relationship that I observe between field galaxies and cluster galaxies in Figure 3.1. This suggests that environmental mechanisms that impact the atomic gas content of a galaxy significantly impact the R_{mol} vs. P_{DE} relation of a galaxy.

As we move from the low def_{HI} panel to the high def_{HI} panel in Fig. 3.4 the contour lines of the cluster sub-samples shift leftwards. This indicates that at higher def_{HI} values, we have more regions with lower P_{DE} values. This could be because Σ_g values are lower for galaxies with higher def_{HI} values. Watts et al. (2023) divided the VERTICO sample into two def_{HI} bins: $\text{def}_{HI} > 0.7$, which is similar to my bottom

panel, and $0.3 > def_{HI} > 0.7$, which is close to my top right panel. They examined the distributions of Σ_{HI} and Σ_{H_2} for both def_{HI} bins. For $def_{HI} > 0.7$, the median $\log(\Sigma_{HI} [M_{\odot}])$ and median $\log(\Sigma_{H_2} [M_{\odot}])$ values are 0.19 ± 0.14 and 0.70 ± 0.09 . For $0.3 < def_{HI} < 0.7$, the median $\log(\Sigma_{HI})$ and median $\log(\Sigma_{H_2})$ values are 0.50 ± 0.07 and 0.77 ± 0.08 . This shows that the environmental effects that reduce the atomic gas content of galaxies also decrease their molecular gas content. The Σ_g values are, therefore, lower in the highest def_{HI} bin, which would likely cause the P_{DE} values to be lower. The highest overlap between the field sample and the cluster sample is in the low def_{HI} bin. This is in line with expectations since HI acts as a proxy for environmental effects of the cluster. I would, therefore, expect the galaxies that have experienced the least cluster environmental mechanisms to be the most similar to isolated field galaxies.

3.2 Star Formation Rate vs. Dynamical Equilibrium Pressure

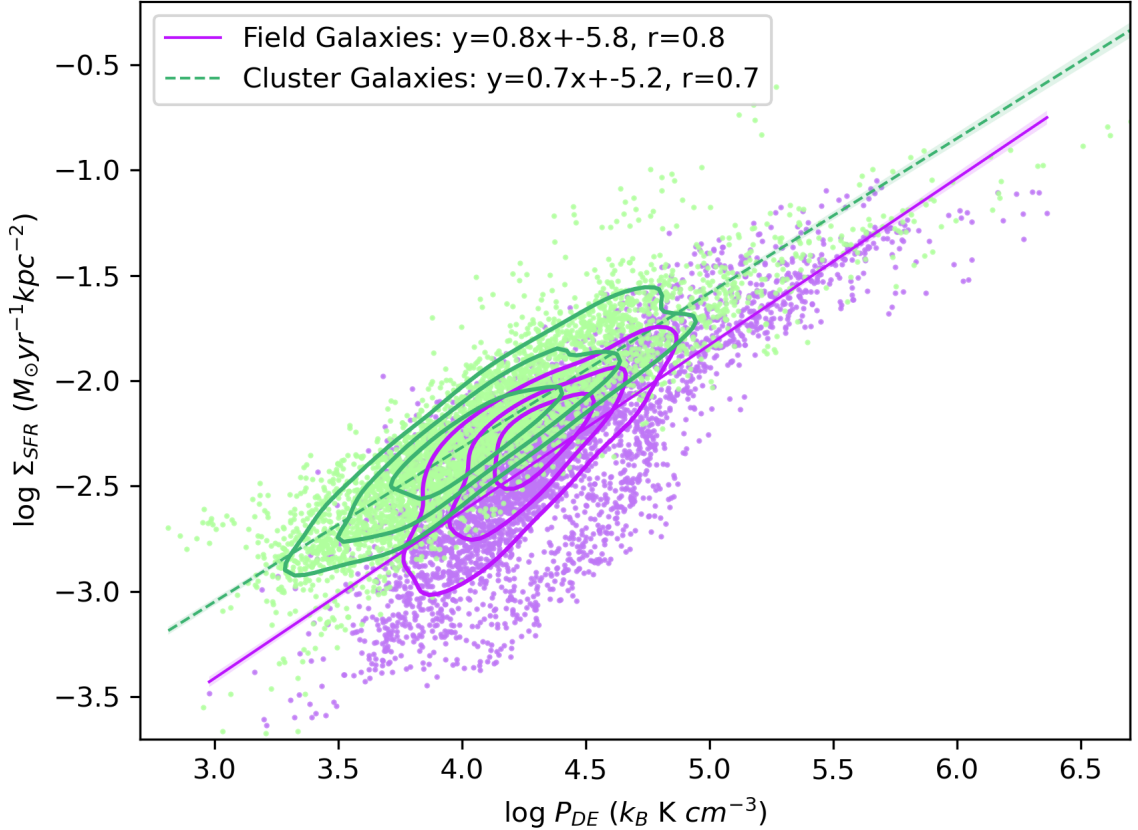


Figure 3.5: Star formation rate as a function of P_{DE} at 1.2 kpc resolution for the field galaxies in purple and the cluster galaxies in green.

Figure 3.5 illustrates that the cluster galaxy sample has slightly higher Σ_{SFR} values at given P_{DE} values than the field sample with similar levels of scatter. The range of my Σ_{SFR} vs. P_{DE} values in Figure 3.5 is very broadly consistent with the Σ_{SFR} vs. P_{DE} values from Ellison et al. (2024) in Figure 3.6. The P_{DE} values in Ellison et al. (2024) assume a fixed value for Σ_{HI} , as Σ_{HI} data is not available at their resolution. This could cause differences between the results of this thesis and the results from

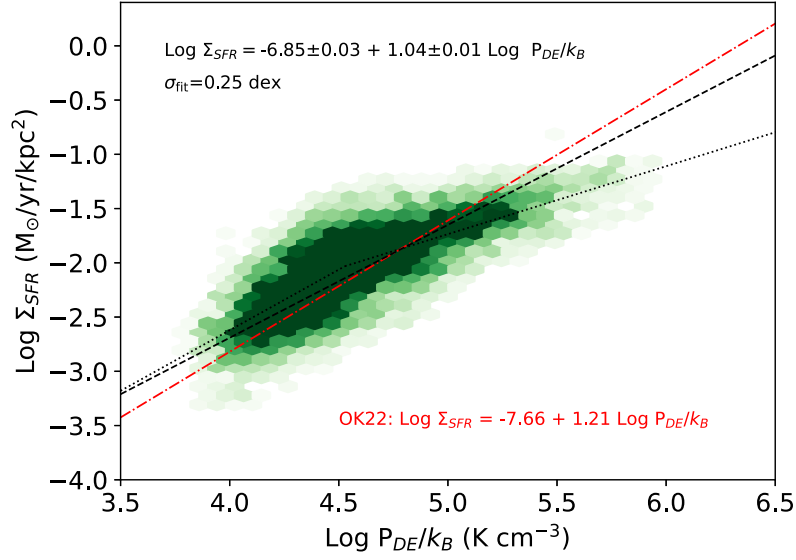


Figure 3.6: Resolved star formation rates surface density vs. dynamical equilibrium pressure for the galaxies in the sample of Ellison et al. (2024). The black dashed line represents the orthogonal distance regression fit of the data. The equation in black at the top left corresponds to the black dashed line. The red dot-dashed line represents the fit to the Ostriker & Kim (2022) simulation. The dotted line represents a broken power-law fit. Image Credit: Ellison et al. (2024)

Ellison et al. (2024).

Figure 3.7 shows a strong difference in the Σ_{SFR} values across def_{HI} bins. As we move from low to high def_{HI} the best-fit lines of the samples do not change drastically. However, the contour lines of the cluster sample move left and down along the best-fit line as we go from low to high def_{HI} in Figure 3.7. Σ_{mol} decreases with increasing def_{HI} as discussed in Section 3.1. This could be the cause for Σ_{SFR} decreasing with increasing def_{HI} as visible in Figure 3.7. The drop in Σ_{SFR} of the cluster sub-samples may be caused by quenching, as it is expected to correlate with higher def_{HI} . Because def_{HI} is representative of environmental influence, this suggests that the stronger the environmental mechanisms that cluster galaxies experience, the lower their P_{DE} values and star formation rates. The contour lines shifting to the left with higher def_{HI} is

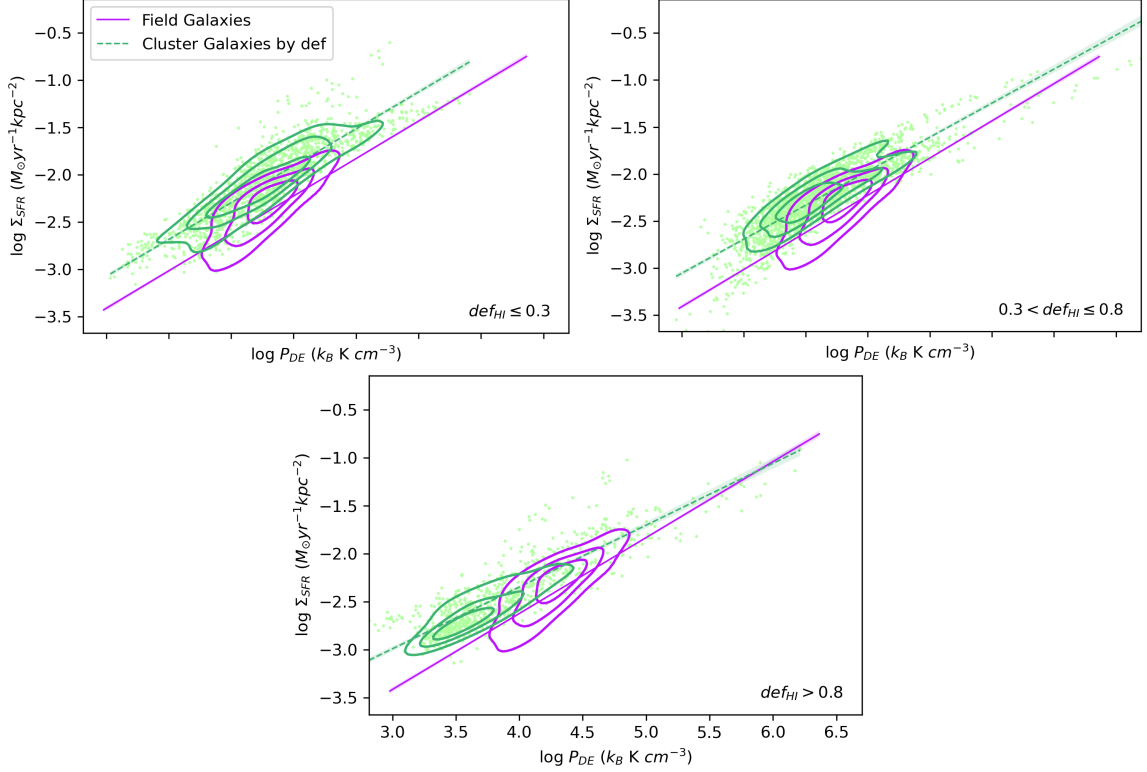


Figure 3.7: The purple contour lines and the purple best-fit line in all the panels correspond to the star formation rate vs. P_{DE} values of the field sample of this thesis and are the same as those in Figure 3.5. The equation of the purple best-fit line is $y = 0.8x - 5.8$. Top left: The green data points, contour lines and best-fit line represent the Σ_{SFR} vs. P_{DE} values of the sub-sample of cluster galaxies that have atomic gas deficiencies ≤ 0.3 . The green best-fit line equation is $y = 0.8x - 5.4$. Top right: The green data points, contour lines and best-fit line represent the Σ_{SFR} vs. P_{DE} values of the sub-sample of cluster galaxies that have atomic gas deficiency values between 0.3 to 0.8. The green best-fit line equation is $y = 0.7x - 5.2$. Bottom: The green data points, contour lines and best-fit line represent the Σ_{SFR} vs. P_{DE} values of the sub-sample of cluster galaxies that have atomic gas deficiency values greater than 0.8. The green best-fit line equation is $y = 0.6x - 4.9$

likely to be driven by the change in Σ_g as discussed in Section 3.1.

3.3 Molecular Gas Depletion Time vs. Dynamical Equilibrium Pressure

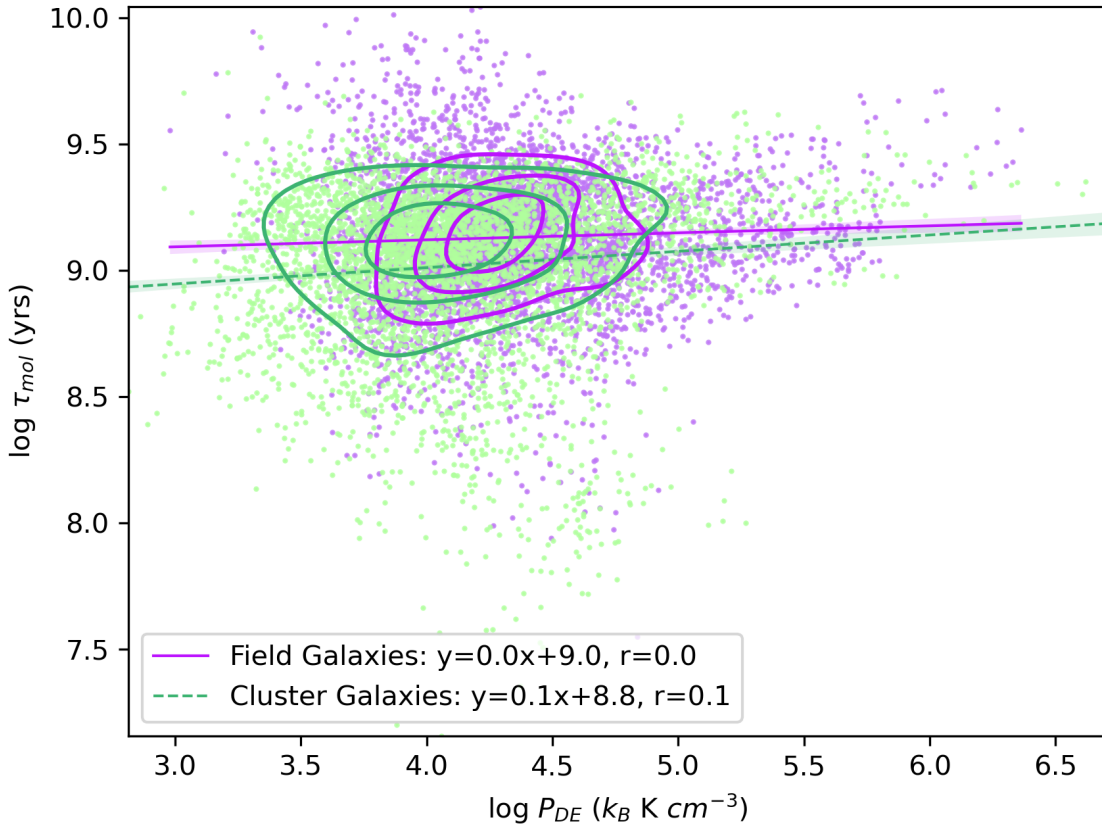


Figure 3.8: Molecular gas depletion time as a function of P_{DE} at 1.2 kpc resolution for the field galaxies in purple and the cluster galaxies in green. The contour lines enclose 25%, 50%, and 75% of the corresponding data points.

Figure 3.8 shows that the cluster galaxies and the field galaxies have comparable τ_{mol} values. The best-fit line for the cluster galaxy sample is only slightly lower than that of the field galaxy sample. Jiménez-Donaire et al. (2023) found the mean

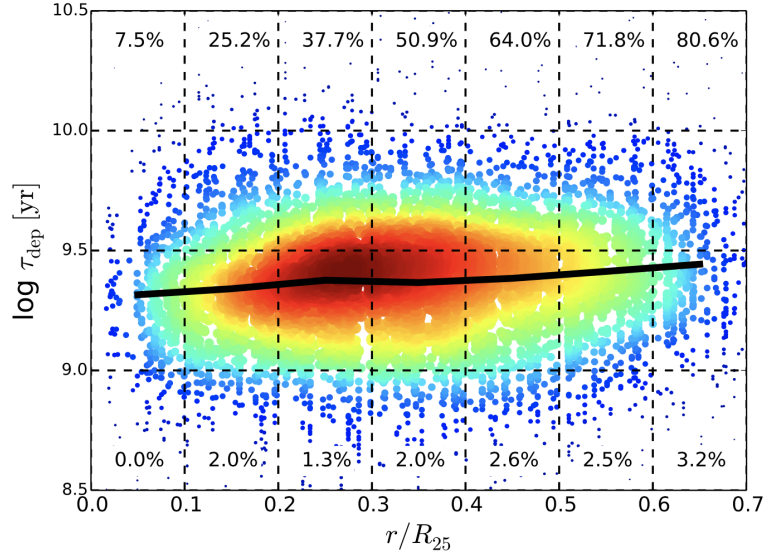


Figure 3.9: Pixel-by-pixel measurements of depletion time as a function of radius for 52 galaxies from the EDGE-CALIFA Survey. The black line is the median value of the depletion time in radial bins. The sizes and colours of the points represent global density of the data points. The percentages at the top of the figure represent the the upper limits of the depletion time, and the percentages at the bottom represent the lower limits. Image Credit: (Utomo et al., 2017)

depletion times of the HERACLES sample used in Bigiel et al. (2008) and Leroy et al. (2013) to be 2 Gyrs. They found the mean depletion time for their sample of VERTICO galaxies to be 1.8 Gyrs. The small difference in τ_{mol} of the two samples in this thesis is roughly consistent with the results of Jiménez-Donaire et al. (2023). However, in this thesis the best-fit line for the cluster sample is slightly lower than that of the field sample, which contradicts Jiménez-Donaire et al. (2023)’s results. In Figure 3.8 τ_{mol} seems to be independent of P_{DE} with the field and cluster gradient values of 0 and 0.1 respectively, and the r values of 0 and 0.1. Utomo et al. (2017) did not initially find a strong trend when they plotted τ_{mol} as a function of P_{DE} , as can be seen in Figure 3.9.

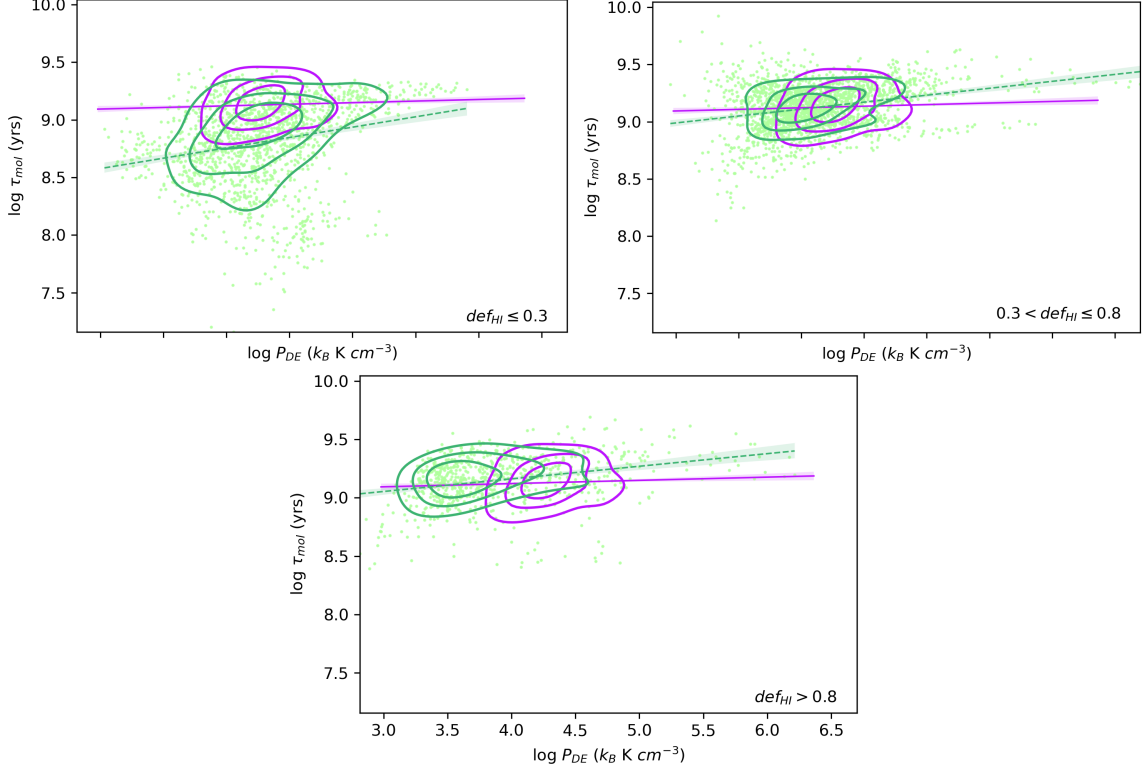


Figure 3.10: The purple contour lines and the purple best-fit line in all the panels correspond to the molecular gas depletion time vs. P_{DE} values of the field sample of this thesis and are the same as those in Figure 3.8. The equation of the purple best-fit line is $y = 0x + 0.9$. Top left: The green data points, contour lines and best-fit line represent the τ_{mol} vs. P_{DE} values of the sub-sample of cluster galaxies that have atomic gas deficiencies ≤ 0.3 . The green best-fit line equation is $y = 0.2x + 8$. Top right: The green data points, contour lines and best-fit line represent the τ_{mol} vs. P_{DE} values of the sub-sample of cluster galaxies that have atomic gas deficiency values between 0.3 to 0.8. The green best-fit line equation is $y = 0.1x + 8.6$. Bottom: The green data points, contour lines and best-fit line represent the τ_{mol} vs. P_{DE} values of the sub-sample of cluster galaxies that have atomic gas deficiency values greater than 0.8. The green best-fit line equation is $y = 0.1x + 8.7$.

Because HI is a good tracer of environmental effects and played a significant role in the different R_{mol} vs. P_{DE} relations of the samples, I also explored the effect of def_{HI} on τ_{mol} as a function of P_{DE} . The cluster galaxies with $def_{HI} \leq 0.3$ in the top left panel of Figure 3.10 include many regions with very low τ_{mol} values. This drags down the slope of the best-fit line of the cluster sub-sample to $y = 0.2x + 8$. The τ_{mol} values range from 0.01 to 2.9 Gyrs for the low def_{HI} bin. The medium def_{HI} cluster galaxies (top right panel) include some of the highest τ_{mol} values, with the maximum being 8.4 Gyrs, as well as τ_{mol} values lower than those of the field galaxies. The lowest τ_{mol} value in this panel is 0.1 Gyrs. The best-fit line of this cluster sub-sample is $y = 0.1x + 8.6$. The highest def_{HI} galaxies (bottom panel) have less of a vertical spread (0.2-4.9 Gyrs) and a similar best-fit line of $y = 0.1x + 8.7$. The lack of low τ_{mol} values at higher def_{HI} could be the result of decreasing star formation efficiency through quenching by environmental mechanisms in the cluster. Figure 3.7 demonstrated that Σ_{SFR} decreases with increasing def_{HI} . This trend could cause τ_{mol} to increase with def_{HI} , since $\tau_{mol} = \Sigma_{mol}/\Sigma_{SFR}$. In order for this to be the case the decrease in Σ_{SFR} with increasing def_{HI} would have to be greater than the decrease in Σ_{mol} that occurs with increasing def_{HI} (discussed in Section 3.1).

In contrast to the other def_{HI} results (Figure 3.4 & Figure 3.7) the difference between the cluster sub-sample and the field sample is higher for lower def_{HI} in Figure 3.10. The contour lines in Figure 3.10 also shift to the left with increasing def_{HI} ; this means that more regions in galaxies with higher def_{HI} have lower P_{DE} values than do regions in low def_{HI} galaxies similar to in Figure 3.4.

3.4 Global Stellar Mass Comparison of Samples

Figure 3.11 shows that my field galaxy sample and cluster galaxy sample have different global M_\star ranges. My samples, consequently, also have different ranges of global SFR, and global H_2 values as demonstrated in Figure 2.2 and Figure 2.1, respectively. In order to examine if my results are driven by the different ranges of M_\star , I apply the selection criteria of $M_\star > 10^{10} M_\odot$ to both my cluster and field samples. Figure 3.11 shows the M_\star and SFR range of my new M_\star restricted cluster galaxy and field galaxy samples. Both samples now have a more similar range of M_\star values.

In Figure 3.12 I show the change in my results if I use the stellar mass cut of $M_\star > 10^{10} M_\odot$ for both the field and cluster samples. The top-left panel shows the change in R_{mol} vs. P_{DE} caused by the stellar mass cut for the field and cluster samples. The top right panel shows the updated τ_{mol} vs. P_{DE} values, and the bottom panel shows the updated Σ_{SFR} vs. P_{DE} values. In Figure 3.12, the contour lines of the new M_\star restricted samples are very close to the original sample contour lines. Because the original sample contour lines overlap significantly with the M_\star restricted contour lines they can be challenging to visually distinguish, particularly for the field sample. The lack of a significant change of the results illustrated in Figure 3.12 shows that the difference in results I observe between my original field and original cluster samples is unlikely to be driven by their differences in M_\star range.

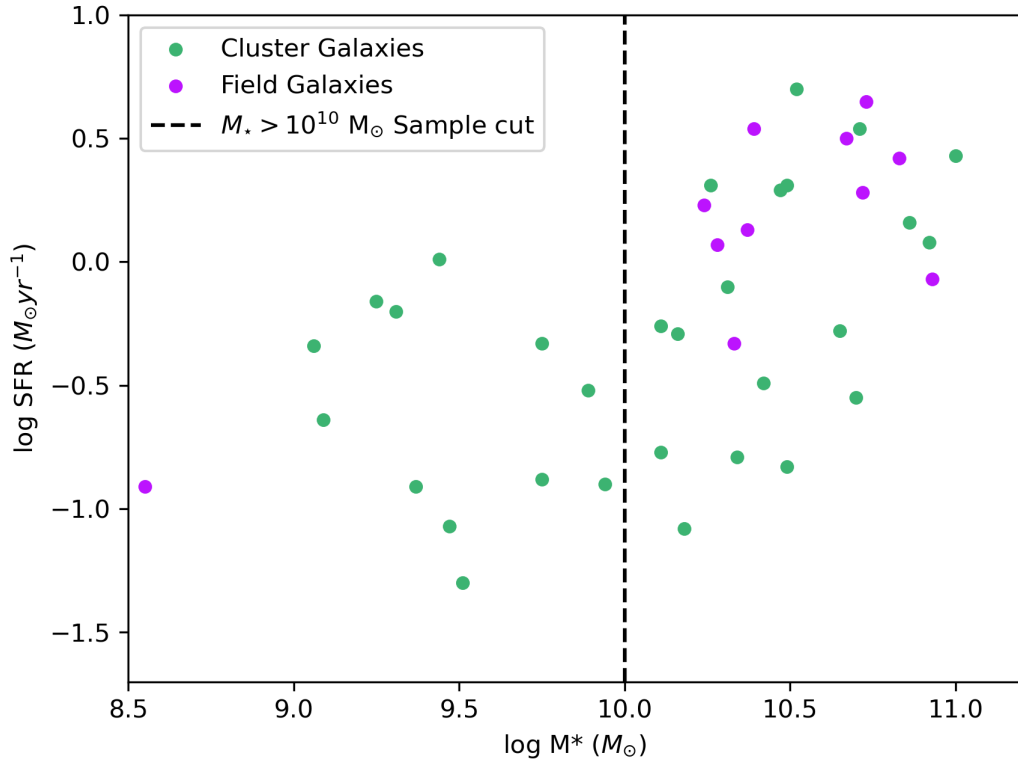


Figure 3.11: The green data points represent the global star formation rate vs. global stellar mass values of the full cluster sample of this thesis. The purple data points represent the values of the field sample of this thesis. The black dashed line at global stellar mass $10^{10} M_\odot$ represents the stellar mass cut I applied to my original samples to obtain the new samples that I analyze in this section. To the right of the black dashed line are the stellar mass values and star formation rates of the galaxies that are included in the reduced samples.

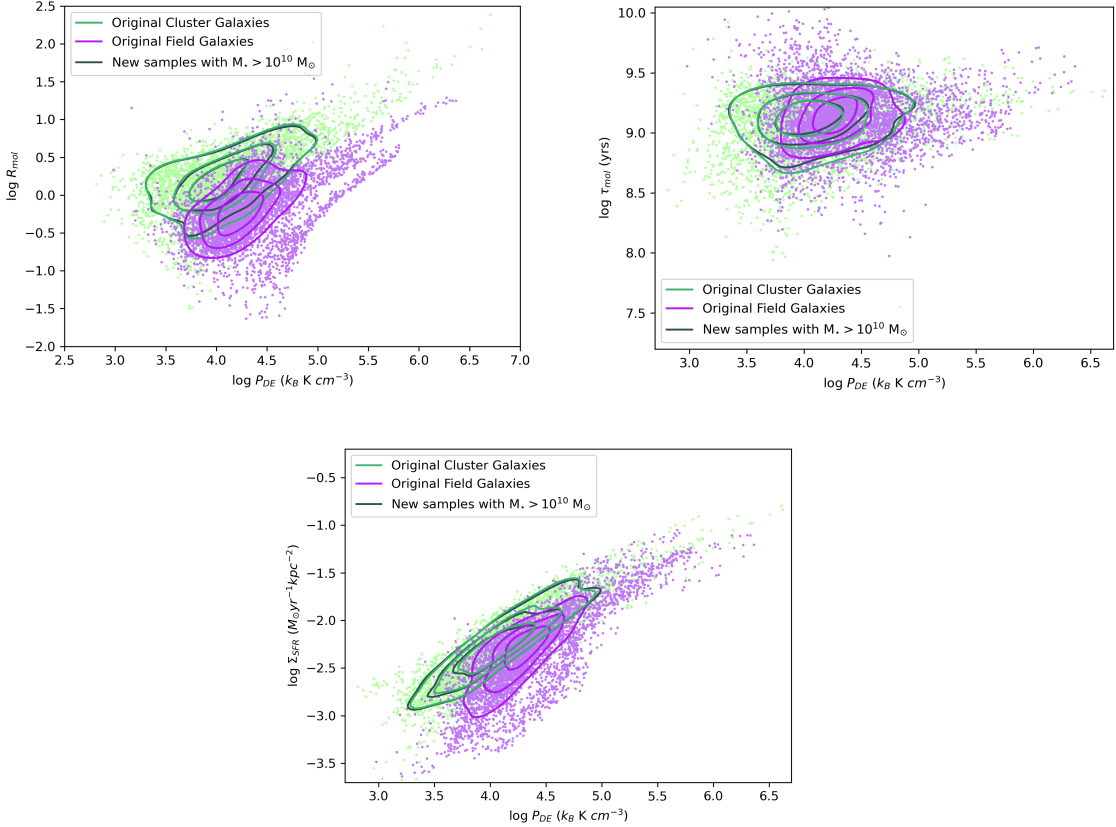


Figure 3.12: Top left: The green data points and contour lines represent the R_{mol} vs. P_{DE} values of the full cluster galaxy sample of this thesis. The purple data points and contour lines represent the R_{mol} vs. P_{DE} values for the full field sample. These are the same as in Figure 3.1. The dark gray contour lines represent the R_{mol} vs. P_{DE} values for the stellar mass restricted ($M_* > 10^{10} M_\odot$) field and cluster samples. Top-right: The green and purple data points and contour lines represent the τ_{mol} vs. P_{DE} values of the original cluster and field samples of this thesis, respectively. They are the same as in Figure 3.8. The dark gray contour lines represent the τ_{mol} vs. P_{DE} values for the stellar mass restricted ($M_* > 10^{10} M_\odot$) field and cluster samples. Bottom: The green and purple data points and contour lines represent the Σ_{SFR} vs. P_{DE} values of the original cluster and field samples of this thesis, respectively. They are the same as in Figure 3.5. The dark gray contour lines represent the Σ_{SFR} vs. P_{DE} values for the stellar mass restricted ($M_* > 10^{10} M_\odot$) field and cluster samples.

Chapter 4

Conclusions & Future Work

4.1 Results of this thesis

A fundamental goal of galaxy evolution is to understand the physics behind the gas properties and star formation in galaxies. Star formation in galaxies shapes the properties and evolution of galaxies. This star formation is significantly influenced by the gas content of galaxies. This is reflected in widely used gas-centric models of galaxy evolution (Dekel et al., 2009; Davé et al., 2011; Lilly et al., 2013), and gas scaling relations such as the resolved Kennicutt-Schmidt relation (Schmidt, 1959; Kennicutt, 1998).

The observationally confirmed linear relationship of R_{mol} as a function of P_{DE} has led to the pressure-regulated feedback models of star formation (Ostriker & Shetty, 2011; Shetty & Ostriker, 2012; Kim et al., 2013; Ostriker & Kim, 2022). If pressure-regulated feedback models encompass foundational physics behind star formation processes in galaxies, the model would hold across different galaxy environments. Consequently, any variation in empirical P_{DE} relationships in different environments

would be well understood. By examining the differences in R_{mol} , Σ_{SFR} , and τ_{mol} as a function of P_{DE} in cluster and field galaxy environments this thesis hopefully enhances our understanding of dynamical equilibrium pressure as a fundamental parameter in star formation in galaxy evolution.

I found R_{mol} vs. P_{DE} values of the cluster galaxy sample to be higher than those of the field galaxy sample. This is likely to be driven by the reduction of the gas content of cluster galaxies by environmental mechanisms, particularly the atomic gas. The Σ_{SFR} vs. P_{DE} and τ_{mol} vs. P_{DE} relationships were similar for cluster galaxies and field galaxies. With increasing atomic gas deficiency of the cluster galaxies we see the following: (1) The P_{DE} values decrease. This is likely to be because the environmental mechanisms that strip the atomic gas content also cause the total gas content of the galaxies to decrease. (2) The R_{mol} vs. P_{DE} line shifts towards higher R_{mol} values. The drop in atomic gas content caused by environmental mechanisms is likely to be more significant than the drop in molecular content or total gas content that the mechanisms cause. This would cause the R_{mol} values to increase relative to the P_{DE} values. (3) The Σ_{SFR} and P_{DE} values both decrease along the cluster best-fit line. This is likely to be because galaxies that experience more atomic gas stripping through environmental mechanisms also experience higher drops in molecular gas and total gas. (4) The depletion time increases and the range of depletion time values decreases.

My thesis shows that the environmental mechanisms that galaxies in clusters experience play a significant role in determining their gas and star formation properties. The effects of environmental mechanisms demonstrated in this thesis must, therefore,

be accounted for when considering pressure-regulated feedback models in galaxy evolution.

4.2 Future Work

The next step I will take in my research is to conduct a more rigorous statistical analysis of my results. For all my work that includes linear regression analysis I will use the Bayesian model LINMIX (Kelly, 2007) to obtain my best-fit line estimate. LINMIX accounts for the measurement errors of the data and would, therefore, enhance my current analysis. I will also examine the one variable distributions of each of my parameters of interest (P_{DE} , R_{mol} , τ_{mol} , Σ_{SFR} , Σ_{HI} , Σ_{mol} , Σ_g) for my cluster galaxy sample, and field galaxy sample. I will do so by performing the Kolmogorov Smirnov test on each of the parameters to determine if variables for the cluster sample vs the field sample are consistent with being drawn from different populations. An examination of the one-dimensional distribution of the gas content for every def_{HI} bin will also provide me with more insight into the driving forces behind my results relative to approximate interpretations based on mean gas values.

When I compared molecular depletion time as a function of P_{DE} the best-fit lines I obtained in Figure 3.8 suggested that τ_{mol} is independent of P_{DE} . The initial inspection of τ_{mol} as a function of radius in Utomo et al. (2017) did not reveal significant trends as discussed in Section 3.3. However, with further analysis Utomo et al. (2017) found the depletion time to be shorter at the center of galaxies with a mean τ_{mol} of 1 Gyr than the disks of galaxies with a mean τ_{mol} of 2.4 Gyr. Because the central region of galaxies typically have higher P_{DE} values than the outer regions of galaxies, this result would lead me to expect higher τ_{mol} with lower P_{DE} . It is, therefore, likely

that in order to reveal a P_{DE} dependence in my results I would have to conduct further analysis. I will, therefore, examine if binning the τ_{mol} vs. P_{DE} data for each of my samples reveals any underlying trends. I will also separate the pixels from the central region of the galaxy from the pixels in the outer disks in order to see if there are any hidden trends in either of these categories. I will also examine the τ_{mol} vs. P_{DE} relations of individual galaxies in each of my samples.

A possible question that arises from this thesis is if the differences in results I observe between cluster galaxies and field galaxies are a result of differences in environment or if they are caused by biases in other properties of the VERTICO vs. HERACLES samples. Dr. Sara L. Ellison revealed in discussion that she found no significant differences in SFR vs. P_{DE} between the PHANGS galaxy field sample and the VERTICO cluster galaxy sample. I have found our two calculation methods of P_{DE} to be relatively consistent. I will, therefore, next compare SFR vs. P_{DE} for the PHANGS and HERACLES samples in order to examine what may potentially cause differences in the relations for both samples, despite them both being field galaxy samples. I will also compare the global SFR, total M_* , and total molecular gas mass of both samples in case any of these parameters significantly vary between the two samples.

In this thesis, I find that def_{HI} , which I use as a proxy for environmental effects, plays a significant role in all my results. It would, therefore, be valuable to further investigate the role of the environment by plotting my cluster galaxies in a phase space diagram with cluster-centric radius on the x-axis, and velocity normalized by velocity dispersion on the y-axis. I also hope to incorporate ram pressure calculations into my analysis. My future work aims to enhance our understanding of the causes

behind the results in this thesis and contribute to our understanding of the physics behind how the environment of a galaxy influences its properties.

Appendix A

R_{mol} vs. P_{DE} for Individual Galaxies

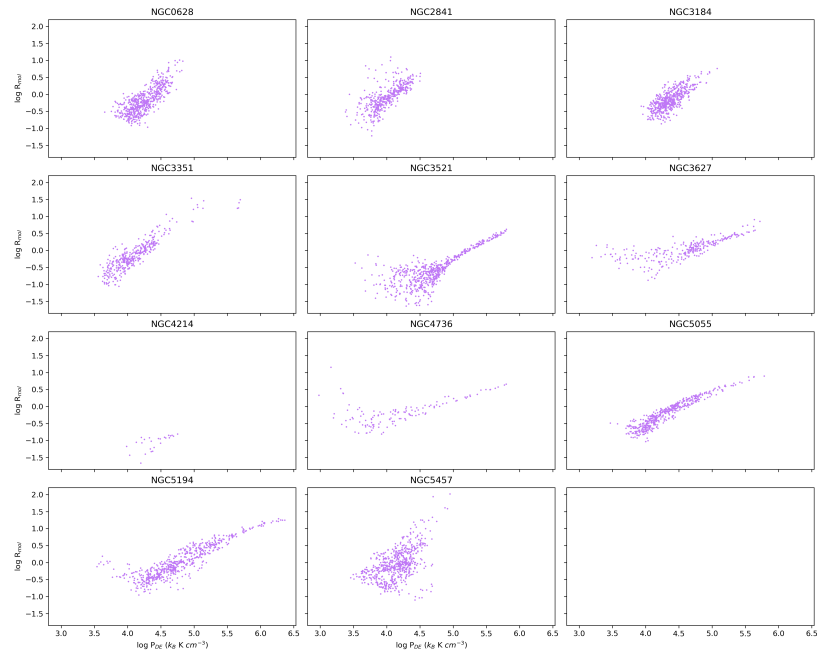


Figure A.1: Molecular gas to atomic gas ratio vs. dynamical equilibrium pressure for every galaxy in the field sample at 1.2 kpc resolution

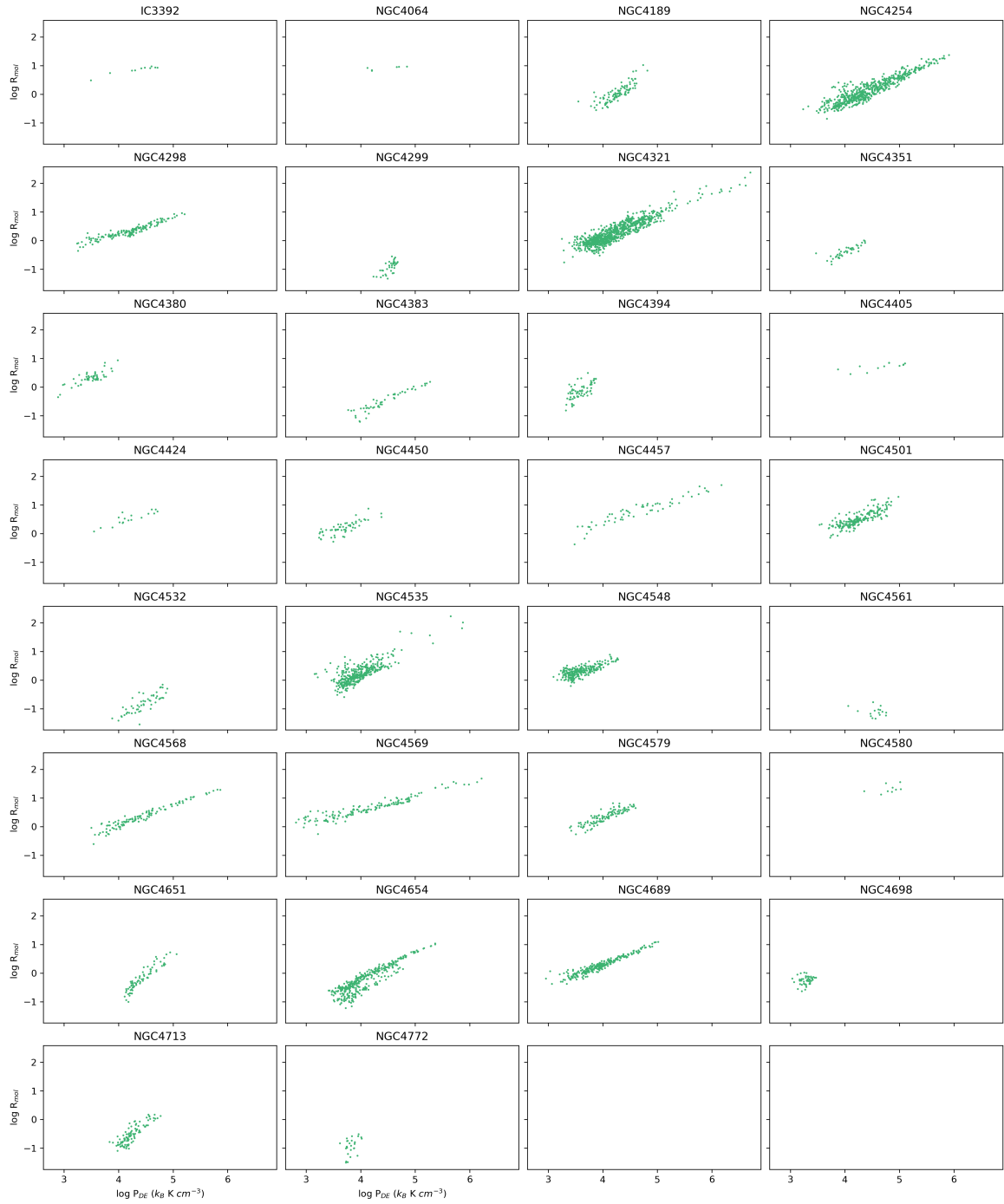


Figure A.2: Molecular gas to atomic gas ratio vs. dynamical equilibrium pressure for every galaxy in the cluster sample at 1.2 kpc resolution

Bibliography

- Accurso, G., Saintonge, A., Catinella, B., et al. 2017, MNRAS, 470, 4750
- Baker, W. M., Maiolino, R., Bluck, A. F. L., et al. 2022, MNRAS, 510, 3622
- Balogh, M. L., Navarro, J. F., & Morris, S. L. 2000, ApJ, 540, 113
- Balogh, M. L., Schade, D., Morris, S. L., et al. 1998, ApJ, 504, L75
- Barrera-Ballesteros, J. K., Sánchez, S. F., Heckman, T., et al. 2021, MNRAS, 503, 3643
- Bekki, K., Couch, W. J., & Shioya, Y. 2002, ApJ, 577, 651
- Bemis, A. & Wilson, C. D. 2019, AJ, 157, 131
- Bertoldi, F. & McKee, C. F. 1992, ApJ, 395, 140
- Bigiel, F., Leroy, A., Walter, F., et al. 2008, AJ, 136, 2846
- Bigiel, F., Leroy, A. K., Jiménez-Donaire, M. J., et al. 2016, ApJ, 822, L26
- Blitz, L. 1993, in Protostars and Planets III, ed. E. H. Levy & J. I. Lunine, 125
- Blitz, L. & Rosolowsky, E. 2004, ApJ, 612, L29

- Blitz, L. & Rosolowsky, E. 2006, *ApJ*, 650, 933
- Böhringer, H., Briel, U. G., Schwarz, R. A., et al. 1994, *Nature*, 368, 828
- Bolatto, A. D., Leroy, A. K., Rosolowsky, E., Walter, F., & Blitz, L. 2008, *ApJ*, 686, 948
- Bolatto, A. D., Wolfire, M., & Leroy, A. K. 2013, *ARA&A*, 51, 207
- Boselli, A., Boissier, S., Heinis, S., et al. 2011, *A&A*, 528, A107
- Boselli, A., Fossati, M., Ferrarese, L., et al. 2018, *A&A*, 614, A56
- Boselli, A. & Gavazzi, G. 2006, *PASP*, 118, 517
- Brown, T., Roberts, I. D., Thorp, M., et al. 2023, *ApJ*, 956, 37
- Brown, T., Wilson, C. D., Zabel, N., et al. 2021, *ApJS*, 257, 21
- Brunetti, N., Wilson, C. D., Sliwa, K., et al. 2021, *MNRAS*, 500, 4730
- Caldú-Primo, A., Schrubba, A., Walter, F., et al. 2013, *AJ*, 146, 150
- Cano-Díaz, M., Sánchez, S. F., Zibetti, S., et al. 2016, in *The Interplay between Local and Global Processes in Galaxies*, ed. S. F. Sanchez, C. Morisset, & G. Delgado-Inglada, 60
- Carroll, B. W. & Ostlie, D. A. 2017, *An introduction to modern astrophysics*, Second Edition
- Cayatte, V., van Gorkom, J. H., Balkowski, C., & Kotanyi, C. 1990, *AJ*, 100, 604
- Chamaraux, P., Heidmann, J., & Lauqué, R. 1970, *A&A*, 8, 424

- Chung, A., van Gorkom, J. H., Kenney, J. D. P., Crowl, H., & Vollmer, B. 2009, *AJ*, 138, 1741
- Combes, F. & Becquaert, J. F. 1997, *A&A*, 326, 554
- Condon, J. J. & Ransom, S. M. 2016, *Essential Radio Astronomy*
- Cox, D. P. 2005, *ARA&A*, 43, 337
- Davé, R., Finlator, K., & Oppenheimer, B. D. 2011, *MNRAS*, 416, 1354
- Davis, T. A., Alatalo, K., Bureau, M., et al. 2013, *MNRAS*, 429, 534
- Dekel, A., Birnboim, Y., Engel, G., et al. 2009, *Nature*, 457, 451
- Draine, B. T. 2011, *Physics of the Interstellar and Intergalactic Medium*
- Dressler, A. 1980, *ApJ*, 236, 351
- Dressler, A. 1984, *ARA&A*, 22, 185
- Eke, V. R., Baugh, C. M., Cole, S., et al. 2005, *MNRAS*, 362, 1233
- Ellison, S. L., Pan, H.-A., Bluck, A. F. L., et al. 2024, *MNRAS*, 527, 10201
- Elmegreen, B. G. 1989, *ApJ*, 338, 178
- Elmegreen, B. G. & Parravano, A. 1994, *ApJ*, 435, L121
- Enia, A., Rodighiero, G., Morselli, L., et al. 2020, *MNRAS*, 493, 4107
- Federrath, C. & Klessen, R. S. 2012, *ApJ*, 761, 156
- Ferrarese, L., Côté, P., Cuillandre, J.-C., et al. 2012, *ApJS*, 200, 4

Field, G. B., Blackman, E. G., & Keto, E. R. 2011, MNRAS, 416, 710

Fisher, D. B., Bolatto, A. D., White, H., et al. 2019, ApJ, 870, 46

Fujita, Y. 1998, ApJ, 509, 587

Fujita, Y. & Sarazin, C. L. 2001, ApJ, 563, 660

Fukui, Y. & Kawamura, A. 2010, ARA&A, 48, 547

Gallagher, M. J., Leroy, A. K., Bigiel, F., et al. 2018, ApJ, 858, 90

Gavazzi, G., Boselli, A., Scodreggio, M., Pierini, D., & Belsole, E. 1999, MNRAS, 304, 595

Giovanelli, R. & Haynes, M. P. 1985, ApJ, 292, 404

Girardi, M., Borgani, S., Giuricin, G., Mardirossian, F., & Mezzetti, M. 1998, ApJ, 506, 45

Gómez, P. L., Nichol, R. C., Miller, C. J., et al. 2003, ApJ, 584, 210

Goto, T., Yamauchi, C., Fujita, Y., et al. 2003, MNRAS, 346, 601

Gunn, J. E. & Gott, J. Richard, I. 1972, ApJ, 176, 1

Haynes, M. P., Giovanelli, R., & Chincarini, G. L. 1984, ARA&A, 22, 445

Herrera-Camus, R., Bolatto, A., Wolfire, M., et al. 2017, ApJ, 835, 201

Hester, J. A. 2006, ApJ, 647, 910

Heyer, M. & Dame, T. M. 2015, ARA&A, 53, 583

- Heyer, M., Krawczyk, C., Duval, J., & Jackson, J. M. 2009, *ApJ*, 699, 1092
- Heyer, M. H., Carpenter, J. M., & Snell, R. L. 2001, *ApJ*, 551, 852
- Hsieh, B. C., Lin, L., Lin, J. H., et al. 2017, *ApJ*, 851, L24
- Hughes, A., Meidt, S. E., Colombo, D., et al. 2013a, *ApJ*, 779, 46
- Hughes, A., Meidt, S. E., Schinnerer, E., et al. 2013b, *ApJ*, 779, 44
- Israel, F. P. 1997, *A&A*, 317, 65
- Jiménez-Donaire, M. J., Usero, A., Bešlić, I., et al. 2023, *A&A*, 676, L11
- Johnson, K. E., Leroy, A. K., Indebetouw, R., et al. 2015, *ApJ*, 806, 35
- Kaiser, N. 1986, *MNRAS*, 222, 323
- Kelly, B. C. 2007, *ApJ*, 665, 1489
- Kennicutt, Robert C., J. 1998, *ApJ*, 498, 541
- Kennicutt, R. C. & Evans, N. J. 2012, *ARA&A*, 50, 531
- Keto, E. R. & Myers, P. C. 1986, *ApJ*, 304, 466
- Kim, C.-G., Ostriker, E. C., & Kim, W.-T. 2013, *ApJ*, 776, 1
- Kim, S., Rey, S.-C., Jerjen, H., et al. 2014, *ApJS*, 215, 22
- Kim, W.-T. & Ostriker, E. C. 2007, *ApJ*, 660, 1232
- Koopmann, R. A. & Kenney, J. D. P. 2004, *ApJ*, 613, 866
- Koyama, H. & Ostriker, E. C. 2009, *ApJ*, 693, 1346

- Kruijssen, J. M. D. & Longmore, S. N. 2014, MNRAS, 439, 3239
- Krumholz, M. R. 2021, in Astronomical Society of the Pacific Conference Series, Vol. 528, New Horizons in Galactic Center Astronomy and Beyond, ed. M. Tsuboi & T. Oka, 19
- Krumholz, M. R., Burkhardt, B., Forbes, J. C., & Crocker, R. M. 2018, MNRAS, 477, 2716
- Krumholz, M. R., McKee, C. F., & Klein, R. I. 2005, Nature, 438, 332
- Larson, R. B. 1981, MNRAS, 194, 809
- Larson, R. B., Tinsley, B. M., & Caldwell, C. N. 1980, ApJ, 237, 692
- Lee, B., Chung, A., Tonnesen, S., et al. 2017, MNRAS, 466, 1382
- Leroy, A. K., Bolatto, A. D., Ostriker, E. C., et al. 2015, ApJ, 801, 25
- Leroy, A. K., Sandstrom, K. M., Lang, D., et al. 2019, ApJS, 244, 24
- Leroy, A. K., Schinnerer, E., Hughes, A., et al. 2021, ApJS, 257, 43
- Leroy, A. K., Walter, F., Bigiel, F., et al. 2009, AJ, 137, 4670
- Leroy, A. K., Walter, F., Brinks, E., et al. 2008, AJ, 136, 2782
- Leroy, A. K., Walter, F., Sandstrom, K., et al. 2013, AJ, 146, 19
- Lilly, S. J., Carollo, C. M., Pipino, A., Renzini, A., & Peng, Y. 2013, ApJ, 772, 119
- Lin, L., Pan, H.-A., Ellison, S. L., et al. 2019, ApJ, 884, L33

- Martin, C. & GALEX Team. 2005, in IAU Symposium, Vol. 216, Maps of the Cosmos, ed. M. Colless, L. Staveley-Smith, & R. A. Stathakis, 221
- McKee, C. F. & Ostriker, J. P. 1977, ApJ, 218, 148
- Mei, S., Blakeslee, J. P., Côté, P., et al. 2007, ApJ, 655, 144
- Meidt, S. E. 2016, ApJ, 818, 69
- Mogotsi, K. M., de Blok, W. J. G., Caldú-Primo, A., et al. 2016, AJ, 151, 15
- Mok, A., Wilson, C. D., Knapen, J. H., et al. 2017, MNRAS, 467, 4282
- Molendi, S., Eckert, D., De Grandi, S., et al. 2016, A&A, 586, A32
- Moore, B., Katz, N., Lake, G., Dressler, A., & Oemler, A. 1996, Nature, 379, 613
- Moore, B., Lake, G., & Katz, N. 1998, ApJ, 495, 139
- Moore, B., Lake, G., Quinn, T., & Stadel, J. 1999, MNRAS, 304, 465
- Moretti, A., Paladino, R., Poggianti, B. M., et al. 2020, ApJ, 897, L30
- Nulsen, P. E. J. & Bohringer, H. 1995, MNRAS, 274, 1093
- Oemler, Augustus, J. 1974, ApJ, 194, 1
- Oka, T., Hasegawa, T., Sato, F., et al. 2001, ApJ, 562, 348
- Ostriker, E. C. & Kim, C.-G. 2022, ApJ, 936, 137
- Ostriker, E. C. & Shetty, R. 2011, ApJ, 731, 41
- Postman, M., Franx, M., Cross, N. J. G., et al. 2005, ApJ, 623, 721

- Saintonge, A. & Catinella, B. 2022, *ARA&A*, 60, 319
- Saintonge, A., Wilson, C. D., Xiao, T., et al. 2018, *MNRAS*, 481, 3497
- Salo, H., Laurikainen, E., Laine, J., et al. 2015, *ApJS*, 219, 4
- Sánchez, S. F. 2020, *ARA&A*, 58, 99
- Sánchez, S. F., Rosales-Ortega, F. F., Jungwiert, B., et al. 2013, *A&A*, 554, A58
- Sawada, T., Hasegawa, T., Sugimoto, M., Koda, J., & Handa, T. 2012, *ApJ*, 752, 118
- Schinnerer, E. & Leroy, A. K. 2024, arXiv e-prints, arXiv:2403.19843
- Schmidt, M. 1959, *ApJ*, 129, 243
- Schruba, A., Kruijssen, J. M. D., & Leroy, A. K. 2019, *ApJ*, 883, 2
- Schruba, A., Leroy, A. K., Walter, F., et al. 2011, *AJ*, 142, 37
- Scoville, N. Z. 2013, in *Secular Evolution of Galaxies*, ed. J. Falcón-Barroso & J. H. Knapen, 491
- Scoville, N. Z., Yun, M. S., Clemens, D. P., Sanders, D. B., & Waller, W. H. 1987, *ApJS*, 63, 821
- Sheth, K., Hinz, J., Gil de Paz, A., et al. 2008, *The Spitzer Survey of Stellar Structure in Galaxies (S4G)*, Spitzer Proposal ID #60007
- Shetty, R. & Ostriker, E. C. 2012, *ApJ*, 754, 2
- Solanes, J. M., Manrique, A., García-Gómez, C., et al. 2001, *ApJ*, 548, 97
- Solomon, P. M., Downes, D., Radford, S. J. E., & Barrett, J. W. 1997, *ApJ*, 478, 144

- Stark, A. A. & Brand, J. 1989, *ApJ*, 339, 763
- Sun, J., Leroy, A. K., Ostriker, E. C., et al. 2020a, *ApJ*, 892, 148
- Sun, J., Leroy, A. K., Schinnerer, E., et al. 2020b, *ApJ*, 901, L8
- Sun, J., Leroy, A. K., Schrubba, A., et al. 2018, *ApJ*, 860, 172
- Tacconi, L. J., Genzel, R., & Sternberg, A. 2020, *ARA&A*, 58, 157
- Tamburro, D., Rix, H. W., Leroy, A. K., et al. 2009, *AJ*, 137, 4424
- Tully, R. B. & Shaya, E. J. 1984, *ApJ*, 281, 31
- Utomo, D., Blitz, L., Davis, T., et al. 2015, *ApJ*, 803, 16
- Utomo, D., Bolatto, A. D., Wong, T., et al. 2017, *ApJ*, 849, 26
- Verheijen, M. A. W. & Sancisi, R. 2001, *A&A*, 370, 765
- Walter, F., Brinks, E., de Blok, W. J. G., et al. 2008, *AJ*, 136, 2563
- Warmels, R. H. 1988, *A&AS*, 72, 427
- Watts, A. B., Cortese, L., Catinella, B., et al. 2023, , 40, e017
- White, D. A., Jones, C., & Forman, W. 1997, *MNRAS*, 292, 419
- Wilson, C. D. & Scoville, N. 1990, *ApJ*, 363, 435
- Wilson, C. D., Warren, B. E., Irwin, J., et al. 2011, *MNRAS*, 410, 1409
- Wong, T. & Blitz, L. 2002, *ApJ*, 569, 157
- Yoon, H., Chung, A., Smith, R., & Jaffé, Y. L. 2017, *ApJ*, 838, 81

Zabel, N., Brown, T., Wilson, C. D., et al. 2022, ApJ, 933, 10